

AD-779 917

Optics Research: 1973:2

Robert H. Rediker

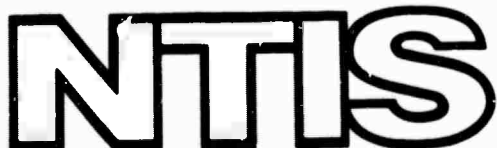
Massachusetts Institute of Technology

Prepared for:

Electronic Systems Division  
Advanced Research Projects Agency

31 December 1973

DISTRIBUTED BY:



National Technical Information Service  
U. S. DEPARTMENT OF COMMERCE  
5285 Port Royal Road, Springfield Va. 22151

**BEST  
AVAILABLE COPY**

AD- 779 917

**DOCUMENT CONTROL DATA - R&D**

(Security classification of title, body of abstract and indexing annotation must be entered when the overall report is classified)

The work reported in this document was performed at Lincoln Laboratory,  
a center for research operated by Massachusetts Institute of Technology.  
This work was sponsored in part by the Advanced Research Projects Agency  
of the Department of Defense (ARPA Order 600) and in part by the Depart-  
ment of the Air Force under Contract F19628-73-C-0002.

This report may be reproduced to satisfy needs of U.S. Government agencies.

**Non-Lincoln Recipients**

**PLEASE DO NOT RETURN**

Permission is given to destroy this document  
when it is no longer needed.

## CONTENTS

<b>Abstract</b>	<b>iii</b>
<b>Introduction</b>	<b>vii</b>
<b>Reports on Optics Research</b>	<b>x</b>
<b>Organization</b>	<b>xiii</b>
<b>I. LASER TECHNOLOGY AND PROPAGATION</b>	<b>1</b>
<b>A. CW Propagation</b>	<b>1</b>
1. CW Propagation Through an Aerosol	1
2. Results of Laboratory Experiments on CW Thermal Blooming	2
<b>B. Pulse Propagation</b>	<b>7</b>
1. Theory	7
2. Experiments	21
<b>C. Effects</b>	<b>29</b>
1. Double-Pulse Pressure and Impulse Measurements	29
2. Hydrodynamic Effects in Double-Pulse Measurements	33
3. Empirical Modeling of Vapor Sphere Expansion from Laser-Exploded Water Droplets	43
4. Abel Inversion Program	44
<b>D. Devices</b>	<b>45</b>
1. Dual 500-J Electron-Beam Laser	45
2. Other Lasers	47
<b>II. OPTICAL MEASUREMENTS AND INSTRUMENTATION</b>	<b>61</b>
<b>A. Triangular Scanning MTF Interferometer</b>	<b>61</b>
1. MTF Interferometric Measurements	61
2. Angle-of-Arrival and Nonimaging Tracker Application of the Interferometer	63

## INTRODUCTION

### I. LASER TECHNOLOGY AND PROPAGATION

For CW laser propagation through a continental aerosol distribution, we can approximate the rms deflection of a laser beam relative to the diffraction spreading and find the effect to be small for a 1-kW beam of 2-cm diameter ( $y_{\text{total}}/y_{\text{diff}} = 1.4 \times 10^{-2}$ ) over a kilometer path. However, since it scales as power/diameter, it can be significant for larger devices.

Further results have been obtained in the laboratory experiment on CW laser thermal blooming. The addition of a nonoptimum phase profile to the near-field laser beam resulted in a 50-percent improvement of the far-field peak irradiance. The peak irradiance on target was observed to decrease when the laser power was increased beyond a critical value. An improved method for adding the desired phase profile to the laser beam involves a pair of cylindrical lenses and a pair of spherical lenses.

The effect of pulse trains on laser propagation has been studied for a few representative cases, showing that for the same total energy thermal blooming is relatively insensitive to the pulse forms.

The effect of a precursor preceding the second pulse by more than three hydrodynamic times is being studied using a double-pulse program. Results indicate that the second pulse can experience substantial blooming when the energy of the precursor is large.

We have developed a propagation code that includes one step of time integration as well as three space dimensions. Calculations of blooming for square apertures have been carried out and compared with circular apertures.

Numerical computation has shown evidence of Brueckner-type dynamic instabilities in thermal blooming of pulsed laser beams. Further exploration is planned to determine whether the effects of turbulence can be amplified to produce these instabilities.

Multiple-scattering calculations have been carried out for propagation of laser pulse through a path in a fog cleared by a precursor. The rms deflection of this second pulse is proportional to the third power of  $r_m$ , the peak value of the fog drop size. Thus, for fogs of considerable water density and  $r_m \sim 2 \mu\text{m}$ , spreading can be significant. The existing Bradley-Herrmann propagation code is being adapted to include propagation through a fog or aerosol.

The absorption of a laser beam by a saturable medium has been examined. The steady-state absorption of a focused beam by a simple three-level system is shown to be equivalent to that of a saturable absorber. This differential equation has been solved numerically for several different conditions. The effects of focusing are significant.

Saturation experiments have been performed with a focused 10.6- $\mu\text{m}$  laser beam in a 5-in cell containing 500 torrs  $\text{CO}_2$  and 250 torrs argon. For these conditions, the linear absorption coefficient was  $1.8 \times 10^{-3} \text{ cm}^{-1}$  and the transmission of laser energy as a function of incident intensity indicated the saturation intensity was from 1 to  $2 \times 10^5 \text{ W/cm}^2$ .

Breakdown experiments were done at 1.06  $\mu\text{m}$  and indicate  $\approx \lambda^{-2}$  scaling for both clean and dirty air thresholds.

Growth dynamics for particle-induced air breakdown were studied to obtain plasma growth rates and absorption depths as a function of intensity. At lower intensities the velocities increase linearly proportional to the intensity  $I$ ; at higher intensities the axial velocity varies roughly as  $I^{1/3}$  in agreement with planar LSD wave theory.

Measurements of peak surface pressure and impulse delivered to aluminum and carbon targets are reported in which two CO<sub>2</sub> laser pulses separated by a variable time delay were used. Delay times for recovery of peak pressure and impulse to single-pulse values were observed to be about 1 msec for the conditions of the experiment.

Results are presented from an experimental examination of the plasma environment produced by irradiation of an aluminum target with two 10.6- $\mu\text{m}$  laser pulses separated in time. Plasma diagnostics include interferometric measurements of neutral and electron density, cross-beam 10.6- $\mu\text{m}$  absorption measurements, and fast streak photography of the luminous front motion.

An empirical relationship has been determined of the time development of the radial growth of the vapor sphere surrounding a water droplet that has been irradiated with a high-intensity 10.6- $\mu\text{m}$  laser pulse.

For a cylindrically symmetric density variation in a material of uniform composition, a numerical approach based on linear splines is used to obtain the density profile from interferometric data. The accuracy of this method has been examined for various test cases.

The dual 500-J e-beam laser is in the final stages of checkout. The device is complete except for the automation of certain auxiliary sequencers. Each laser has been tested independently and has operated successfully with good beam quality. Double-pulse operation has been achieved. The two-pulse laser facility has been constructed to study propagation and target interaction phenomena for an arbitrary interpulse separation.

Calculations indicating the feasibility of an electric discharge H<sub>2</sub>-HF laser are described. Components have been ordered for a 60-J e-beam-initiated HF laser. An intense electron beam will be propagated nearly collinearly with the laser axis through a mixture of SF<sub>6</sub> and C<sub>2</sub>H<sub>6</sub>. The e-beam will be confined by an axial magnetic field. Computer studies are being made to aid in obtaining maximum uniformity of this field. The laser is expected to be operational next reporting period.

Performance of our transverse-discharge HF laser was improved from 0.13 J to 2.25 J output by (1) minimizing the combined inductance of the Marx bank and laser, and (2) changing the hydrogen donor from H<sub>2</sub> to C<sub>2</sub>H<sub>6</sub>. Further increases can be expected by increasing the input electrical energy with a commercially obtained Marx bank to be delivered shortly.

Parts have been ordered for construction of a 10-J H<sub>2</sub>-F<sub>2</sub> flashlamp-initiated laser. Assembly will begin shortly.

An HF kinetics program is being developed for the purpose of predicting the performance of our high-energy HF lasers. The Runge-Kutta method is being used.

Detailed results on  $^{12}\text{C}^{18}\text{O}_2$ ,  $^{13}\text{C}^{16}\text{O}_2$ , and  $^{13}\text{C}^{18}\text{O}_2$  isotope lasers will be published in the February 1974 issue of the Journal of Molecular Spectroscopy. Experiments with  $^{12}\text{C}^{16}\text{O}^{18}\text{O}$  and  $^{13}\text{C}^{16}\text{O}^{18}\text{O}$  isotopes and improved grating-controlled lasers will be continued.

## II. OPTICAL MEASUREMENTS AND INSTRUMENTATION

A description of the operation of the new engineered model of the fast scanning MTF interferometer is described. A technique is outlined to use this interferometer both for accurate angle-of-arrival measurements and as a new type of nonimaging tracker.

REPORTS ON OPTICS RESEARCH

1 July through 31 December 1973

PUBLISHED REPORTS

Journal Articles\*

JA No.

4093	Optical "Seeing" Through the Atmosphere by Interferometric Techniques	D. Kelsall	J. Opt. Soc. of Am. <u>63</u> , 1472-1484 (November 1973).
4176	Rapid Interferometric Technique for MTF Measurements in the Visible or Infrared Region	D. Kelsall	Appl. Opt. <u>12</u> , 1398-1399 (July 1973).
4192	Variable Pulse-Length Electron Beam CO <sub>2</sub> Laser	S. Marcus H. Kleiman R. W. O'Neil L. C. Pettingill	J. Appl. Phys. <u>44</u> , 4232-4233 (September 1973).
4205	Long-Pulse Breakdown with 10.6-μm Laser Radiation	J. E. Lowder H. Kleiman	J. Appl. Phys. <u>44</u> , 5504-5505 (December 1973)
4218	Phase Compensation for Thermal Blooming	L. C. Bradley J. Herrmann	Appl. Opt. <u>13</u> , 331 (1974)
4256	HgCdTe Varactor Photodiode of cw CO <sub>2</sub> Laser Beats Beyond 60 GHz	D. L. Spears C. Freed	Appl. Phys. Lett. <u>23</u> , 445-447 (October 1973).

\* \* \* \* \*

UNPUBLISHED REPORTS

Journal Articles

JA No.

4147	Aerosol Clearing with a 10.6 μm Precursor Pulse	D. E. Lencioni J. E. Lowder	Accepted by IEEE J. Quantum Electron.
4198	Beam Diagnostics for High Energy Pulsed CO <sub>2</sub> Lasers	R. W. O'Neil H. Kleiman L. C. Marquet C. W. Kilcline D. Northam†	Accepted by Appl. Opt.
4200	The Observation of Diffusion as an Effective Vibrational Relaxation Rate in CO <sub>2</sub>	H. Granek	Accepted by IEEE J. Quantum Electron.

\*Reprints available.

JA No.

4210	Determination of Laser Line Frequencies and Vibrational, Rotational Constants of $^{12}\text{C}^{18}\text{O}_2$ , $^{13}\text{C}^{16}\text{O}_2$ , and $^{13}\text{C}^{18}\text{O}_2$ Isotopes from Measurements of CW Beat Frequencies and Fast HgCdTe Photodiodes and Microwave Frequency Counters	C. Freed A. H. M. Ross* R. G. O'Donnell	Accepted by J. Mol. Spectry.
4230	Infrared Spectroscopy with Tunable Lasers	E. D. Hinkley K. W. Nill F. A. Blum	Book Chapter, <u>Laser Spectroscopy of Atoms and Molecules</u> , edited by Professor H. Walther (Springer-Verlag, West Germany).
4239	Measurement of CO <sub>2</sub> Laser Generated Impulse and Pressure	J. E. Lowder L. C. Pettingill	Accepted by Appl. Phys. Lett.
4255	High Energy CO <sub>2</sub> Laser Pulse Transmission Through Fog	J. E. Lowder H. Kleiman R. W. O'Neil	Accepted by Appl. Phys. Lett.
4258	Experimental Study of Large Effective Fresnel Number Confocal Unstable Resonators	H. Granek A. J. Morency	Accepted by Appl. Opt.
4292	Observation of Hydrodynamic Effects of Thermal Blooming	R. W. O'Neil H. Kleiman J. E. Lowder	Accepted by Appl. Phys. Lett.
4317	Spatial Distribution of Electrons in a High Pressure Plasma Produced by Two-Step Photoionization	J. S. Levine A. Javan*	Accepted by J. Appl. Phys.

Meeting Speeches†MS No.

3631	Precision Heterodyne Calibration	C. Freed D. L. Spears R. G. O'Donnell A. H. M. Ross*	Laser Spectroscopy Conference, Vail, Colorado, 25-29 June 1973, accepted by Proceedings of Conference
3584	High Speed HgCdTe Photodiodes at 10.6 $\mu\text{m}$	D. L. Spears I. Melngailis C. Freed T.C. Harman	Device Research Conference, University of Colorado, Boulder, Colorado, 26-28 June 1973
3602	Infrared Spectroscopy Using Tunable Semiconductor Lasers	A. S. Pine K. W. Nill E. D. Hinkley R. S. Eng	17th Conference on Analytical Chemistry in Nuclear Technology, Gatlinburg, Tennessee, 23-25 October 1973
3641	Use of Gyro Technology to Measure Small Random Angular Motion	G. Bukow E. Salamin*	AIAA, Key Biscayne, Florida, 20-22 August 1973

\* Author not at Lincoln Laboratory.

† Titles of Meeting Speeches are listed for information only. No copies are available for distribution.

MS No.

3664	The Dynamics of Particle Induced Air Breakdown in a 10.6 $\mu\text{m}$ Laser Beam	D. E. Lencioni L. C. Pettingill	26th Annual Gaseous Electronics Conference, Madison, Wisconsin, 16-19 October 1973
3665	Feasibility of Electrically-Excited H <sub>2</sub> -HF Laser	R. M. Osgood	
3689	Pulsed 10.6 $\mu\text{m}$ Laser Generated Impulse and Pressure Measurements	J. E. Lowder L. C. Pettingill	DOD Laser Effects/Hardening Conference, Monterey, California, 23-26 October 1973

## ORGANIZATION

### OPTICS DIVISION

R. H. Rediker, *Head*  
L. B. Anderson, *Associate Head*  
M. J. Hudson, *Assistant*

### LASER TECHNOLOGY

S. Edelberg, *Leader*  
L. C. Marquet, *Associate Leader*

Bradley, L. C.	Kafalas, P.	Osgood, R. M.
Brennan, M. J.	Kilcline, C. W.	Pettingill, L. C.
Bushee, J. F., Jr.	Kleiman, H.	Pike, H. A.
Ferdinand, A. P., Jr.	Lencioni, D. E.	Pirroni, J. S.
Finne, P. G.	Levine, J. S.	Pitta, R. F.
Fauche, D. G.	Lower, J. E.	Scott, W. L., Jr.
Granek, H.	Marcus, S.	Sher, S. Y.
Herrmann, J.	Morency, A. J.	Stiehl, W. A.
Joannaon, J. Q.	O'Neil, R. W.	

### ADVANCED SENSORS

J. O. Dimmick, *Leader*  
E. S. Cotton, *Associate Leader*  
T. M. Quist, *Assistant Leader*

Ariel, E. D.	Kelsall, D.	Sample, J. O.
Baukus, J. P.	Keyen, P. J.	Scoular, W. J.
Bielinski, J. W.	Ku, R. T.	Sullivan, F. M.
Corbosiero, D. M.	McPherson, R. D.	Theriault, J. R.
Dickey, D. H.	Nork, L. P.	Thomas, M. A.
Ellis, R. H.	Perry, F. H.	Ziegler, H. L.
Fulton, M. J.	Rotstein, J.	Zwicker, H. R.
Hinckley, E. D.		

### OPTO-RADAR SYSTEMS

A. B. Gochwendtner, *Leader*  
P. R. Longaker, *Assistant Leader*

Bauer, J. R.	DiMarzio, E. W.	Merrill, E. R.
Billups, H. R.	Dyjak, C. P.	Reis, V. H.
Brownson, J. S.	Edwards, D. M.	Rosato, N. F.
Bryant, B. W.	Garavano, L. A.	Stevens, R. R.
Clay, W. G.	Hull, R. J.	Vernon, H. M., Jr.
Coles, R. M.	Johns, T. W.	Ziemann, H. E.
Cordova, R. J.	McPhie, J. M.	

### LASER SYSTEMS

R. H. Kingston, *Leader*  
L. J. Sullivan, *Associate Leader*

Bates, D. H.	Gilmartin, T. J.	Parker, A. C.
Bicknell, W. E.	Holtz, J. A.	Swezey, L. W.
Capes, R. N., Jr.	Malling, L. R.	Teoste, R.
Daley, J. A., Jr.	Marcpot, J. V.	Valcourt, G. L.
Fiasconaro, J. G.	O'Donnell, R. G.	Zimmerman, M. D.
Freed, C.		

## I. LASER TECHNOLOGY AND PROPAGATION

### A. CW PROPAGATION

#### 1. CW Propagation Through an Aerosol

As a first consideration of the propagation of a CW laser beam through an aerosol we take the case of multiple scattering of the radiation through a density of index spheres whose size we assume to be sufficiently large so that the geometric optics approximation is appropriate. The mean deflection per collision is  $\epsilon = \Delta n/n$  and the rms angle of deflection through a path length  $L$  of index spheres of density  $N_r$  is given by<sup>1</sup>

$$\Theta_r = L^{1/2} [N_r \pi a_r^2(t)]^{1/2} \epsilon$$

where  $a(t)$  is the radius of the vapor sphere surrounding an aerosol particle of initial radius  $r$ . The average squared deflection of the beam due to a number density  $N_r$  of particles of radius between  $r$  and  $r + dr$  is then

$$\overline{y^2}(r) = 4/9 L^3 N_r \pi a_r^2(t) (\Delta n/n)^2 .$$

If we assume that the aerosol particles have reached steady state and all of the heat absorbed from the incident radiation diffuses out into the index sphere, then the mean change in index of refraction of the spheres is given by

$$\Delta n = (n - 1) \frac{\Delta T_{air}}{T_0} = (n - 1) \frac{I(\pi r_{aer}^2 t / (4/3 \pi a_r^3 \rho c_p))}{T_0}$$

where  $\Delta T_{air}$  is the temperature change of the air composing the index sphere,  $n$  is the index refraction of air ( $n - 1 \approx 3 \times 10^{-4}$ ),  $I$  is the incident radiation,  $\pi r_{aer}^2$  is the absorption cross section of the aerosol,  $\rho$  the air density, and  $c_p$  the heat capacity at constant pressure for air. Since the diffusion solution is appropriate, the index sphere expansion is given by

$$a_r^2(t) = \kappa t$$

where  $\kappa$  is the diffusion coefficient for air ( $\kappa = 0.2 \text{ cm}^2/\text{sec}$ ). Hence, we find that the rms deflection is independent of time if the beam cross section is uniform in intensity, even with a wind present,

$$\Delta n = \frac{3 I_0 r_{aer}^2 (n - 1)}{4 \kappa p a_r^2(t) \gamma / (\gamma - 1)}$$

where  $p$  is the ambient air pressure and  $\gamma$  is the specific heat ratio for air. For the aerosol distribution, then,

$$\overline{y^2}(r) = \frac{I^2 L^3 N_r r_{aer}^4 (n - 1/4)^2 \pi}{4 \kappa^2 p^2 (\gamma / \gamma - 1)}$$

and

$$y_{\text{total}} = \left[ \int_{r_{\min}}^{r_{\max}} y^2(r) dr \right]^{1/2} .$$

For an example of a typical continental aerosol we can write<sup>2</sup>  $N(r) = 3r^{-4} N_0 r_{\min}^3$  where  $N_0$  is the total particle density. This gives a value of rms deflection

$$y_{\text{total}} \approx \frac{3^{1/2} \pi^{3/2} N_0^{1/2} (n-1)^{1/2}}{2 \kappa p(\gamma-1) n} (r_{\max} r_{\min})^{1/2}$$

where  $r_{\max} \gg r_{\min}$ .

The diffractive spread of the same beam is  $y_{\text{diff}} = 1.2\lambda/D$ , where  $D$  is the beam diameter, so the relative spread due to the density of the fog compared with diffraction is

$$\frac{y_{\text{total}}}{y_{\text{diff}}} = \frac{3^{1/2} P L^{1/2} N_0^{1/2} (r_{\max} r_{\min})^{1/2}}{D \kappa \lambda p(\gamma-1) \pi^{1/2}} \frac{n-1}{n}$$

with  $P$  being the laser power.

For  $L = 1 \text{ km}$ ,  $D = 2 \text{ cm}$ ,  $N_0 = 10^3 \text{ cm}^{-3}$ ,  $P = 1 \text{ kW}$ , and  $\lambda = 10.6 \mu\text{m}$ ,  $r_{\max} = 20 \mu\text{m}$ ,  $r_{\min} \approx 4 \times 10^{-2} \mu\text{m}$ ,  $p = 1 \text{ atm}$ ,

$$\frac{y_{\text{total}}}{y_{\text{diff}}} = 1.4 \times 10^{-2} .$$

At this level of power and this beam size, the spread due to aerosol scattering is not important; but as CW lasers scale up, the effect could become a significant source of beam distortion. For nonuniform intensity cross sections and in the presence of a cross wind, analysis indicates that more severe, asymmetric distortions would be effected.

L. C. Bradley  
H. Granek

## 2. Results of Laboratory Experiments on CW Thermal Blooming

Some further results have been obtained from the laboratory experiment on CW thermal blooming. The first set of results was reported in the previous Optics Research Report.<sup>3</sup> Also given in Ref. 3 is a complete description of the experimental setup. In brief, a focused 5145-Å laser beam is slewed by a rotating mirror through an absorbing gas ( $\text{NO}_2$  buffered by air), and the amount of thermal blooming is measured by having the slewed beam pass over a pinhole array, behind which is a detector. Certain problems that have been encountered - thermal conduction, nonuniform gas mixing, and laser multimoding - affect the experimental results reported here. These problems are being corrected.

(a) One of the main goals of the laboratory experiment is to verify that phase corrections added to the near field of the laser beam can decrease the amount of thermal blooming caused by index-of-refraction variations in the absorbing medium. A set of zero-power cylindrical lenses will be used to add part of the desired phase contours. At the present time, a set of cylindrical lenses with a good surface figure ( $\lambda/10$ ) is not available. Some data were obtained, however, with a set of lenses with  $\sim 1\lambda$  surface figure.

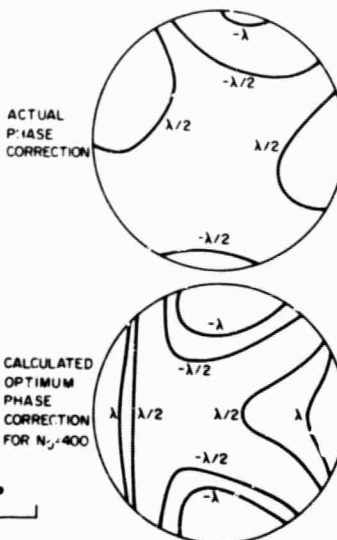
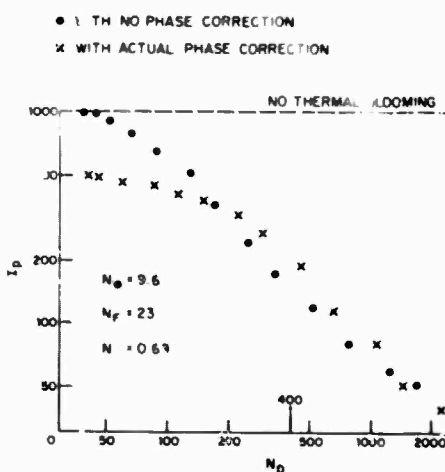


Fig. I-1. Laboratory results which show a decrease in thermal blooming when an appropriate phase profile is added to the near-field laser beam.  $N_D$  is the distortion number, which is inversely proportional to the cross-wind.  $I_p$  is the peak irradiance in the focal plane.

The results are shown in Fig. I-1. The peak irradiance in the focal plane was plotted as a function of distortion number  $N_D^\dagger$  for two cases: when no phase correction was added to the beam and when the phase correction in the upper right-hand corner of the figure was added to the beam. In this experiment, the distortion number was changed by varying the crosswind, so that the dotted line would result in the absence of thermal blooming. At low values of  $N_D$ , where little or no thermal blooming occurs, the phase-corrected beam has a lower peak irradiance than the uncorrected beam because the phase corrections represent aberrations which prevent the beam from focusing into a small spot. As the distortion number is increased, however, the aberrations in the absorbing gas caused by thermal effects begin to cancel the original aberrations in the phase-corrected beam, so that for  $N_D > 170$ , the phase-corrected beam has a higher peak irradiance than the uncorrected one.

On comparison of the experimental points to the dotted line, it is evident that the amount of improvement is small, about 1.5 dB maximum, whereas Bradley and Herrmann<sup>4</sup> predict that as much as 6 dB improvement should be possible. The main reason for the relatively small amount of improvement is that the actual phase correction is far from the optimum one calculated by the propagation code<sup>4</sup> and shown in the lower right-hand corner of Fig. I-1. More improvement is expected once lenses with a good surface figure are obtained and used in future experiments.

(b) The theory developed by Bradley and Herrmann<sup>4</sup> predicts that the peak irradiance on target will actually decrease as the laser power is increased beyond a certain critical power  $P_c$ . This prediction was tested experimentally in the laboratory, and the results are shown in Fig. I-2.

<sup>†</sup> The thermal blooming distortion number is  $N_D = (1/\epsilon \rho c_p) (\partial \epsilon / \partial T) (k \alpha P R / v_o)$ , where  $\epsilon$ ,  $\rho$ ,  $c_p$ ,  $\alpha$ , and  $T$  are the dielectric constant, density, specific heat, absorption coefficient, and temperature of the gas, respectively;  $k$ ,  $P$ , and  $\alpha$  are the wave number, power, and 1/e power radius of the laser beam, respectively;  $R$  is the range; and  $v_o$  is the crosswind velocity.

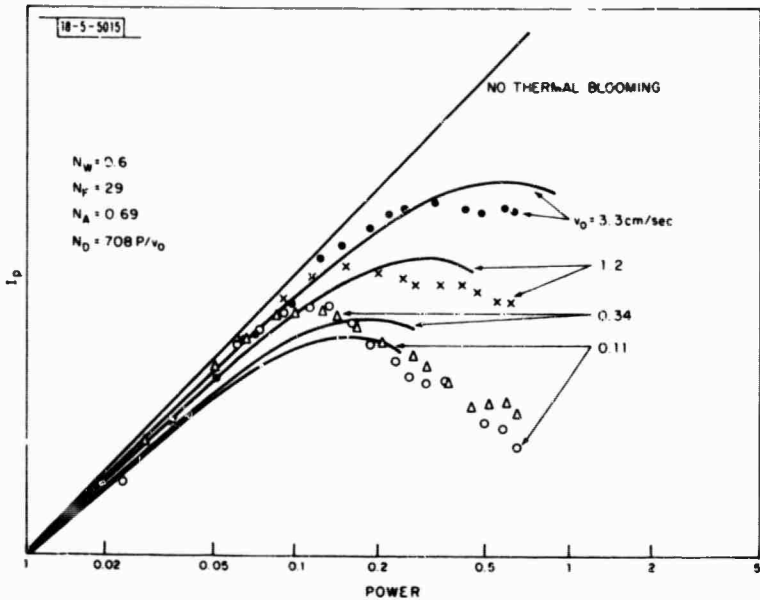


Fig. 1-2. Laboratory results which demonstrate that the peak irradiance on target can actually decrease when the laser power is increased. The discrete points were measured. The solid curves were calculated from theory:  $I_p = (P/A_0) e^{-P/P_c}$ .

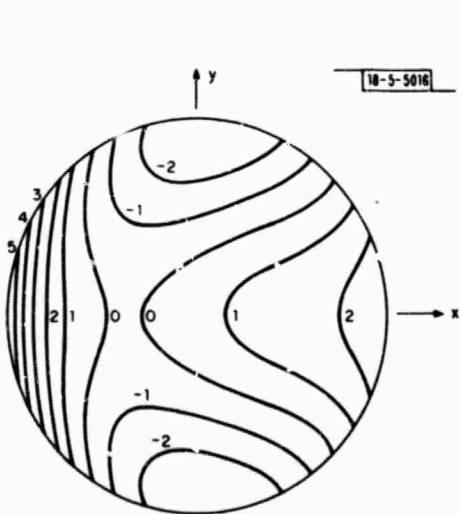


Fig. 1-3. Phase profile calculated to give maximum decrease in thermal blooming for a typical set of laboratory parameters. The contour lines in this and succeeding figures are marked in units of wavelength.

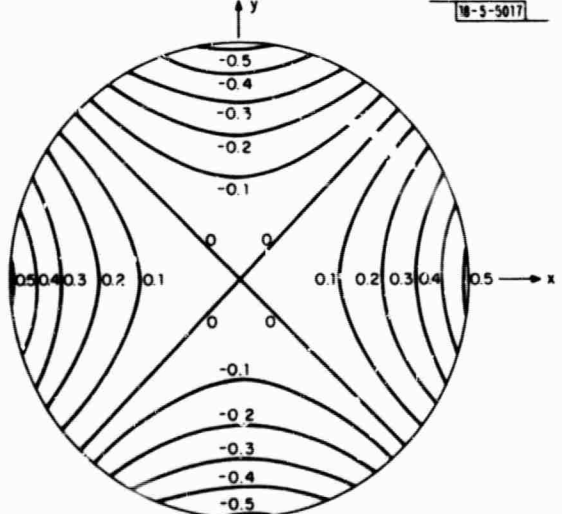


Fig. 1-4. Phase profile provided by a plano-convex and plano-concave cylindrical lens pair. The radius of curvature is 14 cm, the separation is 0.001 cm, and the axes of revolution are at an angle of 0.08°.

along with the theoretical curves. It is to be noticed that for all four values of  $v_o$ ,  $l_p$  does reach a maximum value and then decreases as  $P$  is increased. As expected, the amount of blooming increases as the crosswind  $v_o$  is decreased. However, at the lowest crosswind values, the amount of blooming is independent of  $v_o$ . This independence may be attributed to the fact that in the experiments reported here conduction is the dominant mechanism of heat transfer at low values of  $v_o$ .

Bradley and Herrmann predict curves which may be fitted by the scaling law

$$l_p = \frac{P}{A_o} e^{-P/P_c}$$

$l_p$  is the peak irradiance in the focal plane,  $P$  is the laser power, and  $A_o$  is the beam area in the focal plane in the absence of blooming.  $P_c$  is the critical power at which  $l_p$  reaches a maximum and is given by

$$P_c = 12.4 \frac{2v_o \cdot a}{\alpha kr} \frac{\epsilon \rho c p}{d\epsilon/dT} \frac{1}{\ln(1 + N_\omega)}$$

This theory does not include the effects of conduction, which are obviously present in the experimental results. A simple method of including conduction which gives correct order-of-magnitude results follows. In the expression for  $P_c$ , heat transfer by forced convection is taken into account by the factor  $v_o$ . To take into account additional heat transfer by conduction, one can add to  $v_o$  an effective wind due to conduction,  $v_d = a/t_d$ , where  $t_d$  is the time required for conduction to balance the heat input.  $t_d$  is equal to  $\rho c_p a^2/K$ , where  $K$  is the thermal conductivity of the gas. The curves in Fig. I-2 were calculated using  $(v_o + v_d) = v$  in the expression for  $P_c$ , with  $v_d = 1$  cm/sec.

Quantitatively, the experiment and theory agree to well within a factor of two in the regions where the theory is valid ( $P_c \lesssim 1.5P$  - Ref. 4). Qualitatively, however, the agreement is not good. That is to say, the slope of the experimental curves does not follow a  $P e^{-P/P_c}$  dependence. The experimental curves peak sooner and fall off more slowly. The main cause of the discrepancy is probably the facile manner in which conduction was inserted into the theory, especially in view of the fact that the discrepancy appears to increase as the conduction effect increases. Further experiments in which conduction effects will be reduced are being planned.

(c) Improved methods for adding phase profiles to the laser beam have been devised. Figure I-3 shows a phase plot computed by the propagation code of Bradley and Herrmann. This phase plot is predicted to cause an optimum reduction in thermal blooming for a typical set of parameters in the laboratory experiment. The main feature of the plot is a saddle point. A saddle point can be obtained by a plano-convex and plano-concave cylindrical lens pair of matched curvatures by rotating the axes of revolution slightly with respect to one another. Figure I-4 shows the phase contours that result when the axes of the lenses make an angle of  $0.08^\circ$ .

Figure I-5 shows the difference between the contours of Figs. I-3 and I-4. This difference can be approximated by a matched pair of spherical lenses, one of which is tilted out of the plane perpendicular to the optical axis. Figure I-6 shows an example of the contours available from the spherical lenses. Figure I-7 shows the difference between the contours of Figs. I-5 and I-6. The surface of Fig. I-7 differs from flat by less than  $\lambda/10$  over the whole central portion of the beam, within which more than 70 percent of the energy lies (assuming a Gaussian intensity distribution truncated at the  $1/e^2$  power diameter by the lenses).

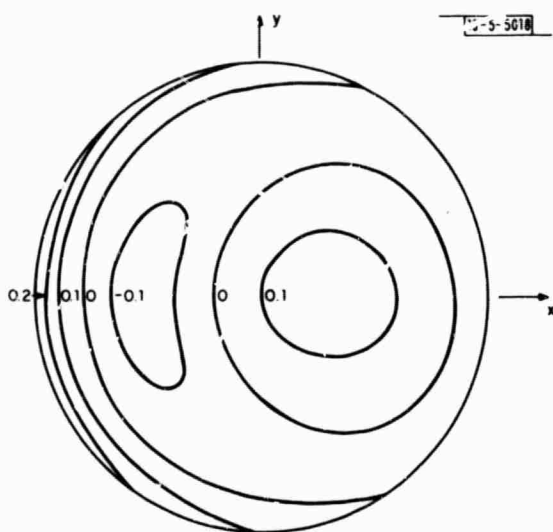


Fig. I-5. Residual phase after the phase contour of Fig. I-3 has been subtracted from that of Fig. I-4.

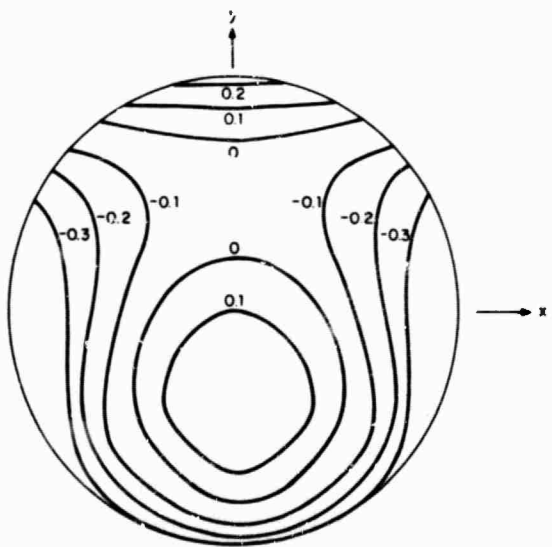


Fig. I-6. Phase profile provided by a plano-convex and plano-concave spherical lens pair. Radius of curvature is 25 cm, the separation is 0.2 cm, and one lens is tilted 3° out of the plane perpendicular to the optical axis.

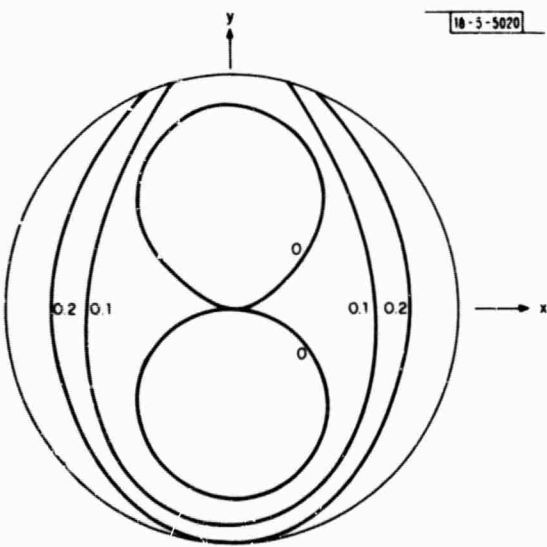


Fig. I-7. Residual phase after the phase contour of Fig. I-5 has been subtracted from that of Fig. I-6.

Thus, a pair of cylindrical lenses in conjunction with a pair of spherical lenses can closely approximate the desired phase contour of Fig. I-3. In addition, the contours of Fig. I-4 show almost pure astigmatism, while those of Fig. I-6 show primarily coma, so that these two aberrations can be separately added to the beam.

D. G. Fouche

## B. PULSE PROPAGATION

### 1. Theory

#### a. Effect of Pulse Trains

##### (1) Gas Dynamics of Pulse Trains

We have performed calculations with the linearized hydrodynamic equations in order to study the gas density change caused by pulse trains. These are compared to the gas density change due to a single pulse with the same total energy. Figure I-8 shows the gas density as a function

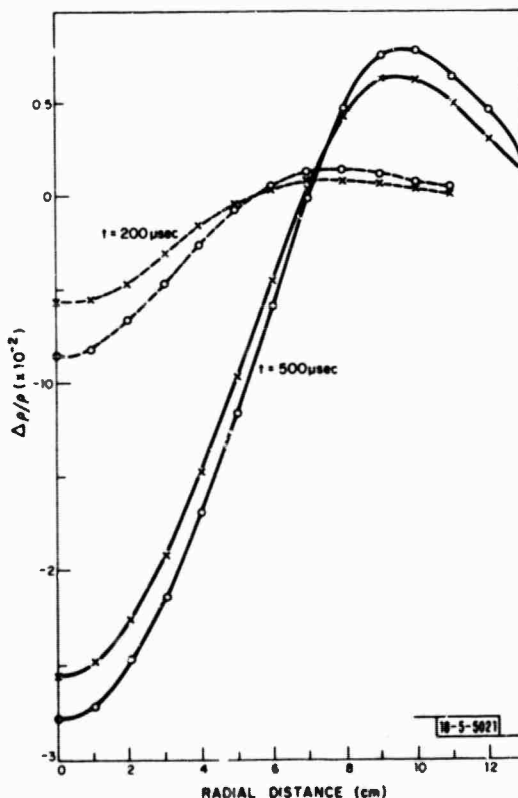


Fig. I-8. Gas density as a function of radius for two times for the pulse train (o) and for a single pulse (x).

of radius for different times for the single pulse and the pulse train for the following conditions:

$$t_2/t_1 = 5, \quad T_p/t_2 = 5, \quad T_p = 500 \mu\text{sec},$$

where  $t_1$  is the duration of a single pulse,  $t_2$  the period, and  $T_p$  is the duration of the pulse train. The beam shape is an infinite Gaussian with  $1/e$  power radius of 6 cm, giving a hydrodynamic time  $t_h = 200 \mu\text{sec}$ . The peak pulse energy density absorbed by the air for each of the two pulse forms is  $8.5 \times 10^{-2} \text{ J/cm}^3$ . As can be seen from Fig. I-8, the gas density changes are not very different at the end of the pulse train ( $t = T_p$ ) and we expect, therefore, that the propagation is insensitive to pulse forms.

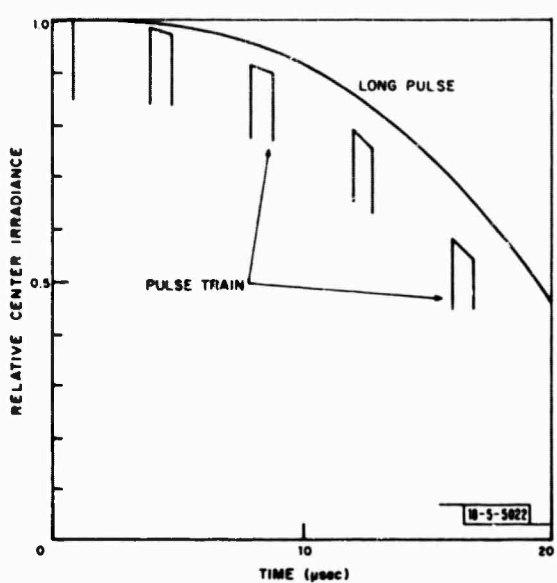


Fig. I-9. Relative center irradiance as a function of time for two pulse forms for mild blooming.

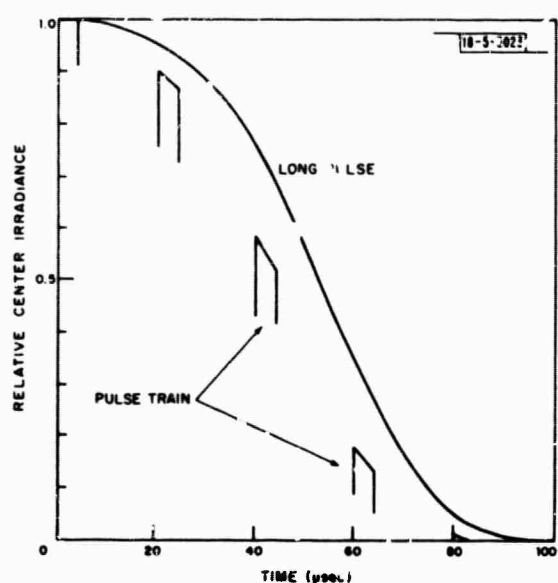


Fig. I-10. Relative center irradiance as a function of time for two pulse forms for strong blooming.

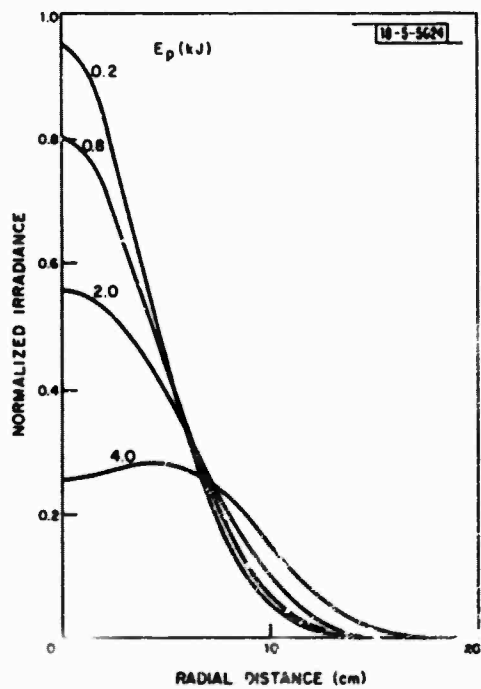


Fig. I-11. Normalized irradiance in the focal plane of the second pulse as a function of radius for some values of energy in the first pulse.

## (2, Propagation of Pulse Trains

The effect of a pulse train on propagation is shown in Fig. 1-9 for the following conditions: pulse energy = 80 kJ, range = 5 km, beam quality parameter  $\beta = 2$ ,  $c = 10^{-3} \text{ cm}^{-1}$ , and a hydrodynamic time  $t_h = 140 \mu\text{sec}$ , for a single pulse 20  $\mu\text{sec}$  long and a train of five pulses with the same total energy, each pulse .8  $\mu\text{sec}$  long. The pulse train shows slightly more blooming than the single pulse as a consequence of the hydrodynamic results shown above.

The same results hold for a pulse with strong thermal blooming, shown in Fig. 1-10, for a pulse energy of 20 kJ and a pulse duration  $T_p = 100 \mu\text{sec}$  long. Other parameters are the same as in the previous case.

J. Herrmann

### b. A Double-Pulse Program

A propagation program has been written which handles double pulses. The first pulse (precursor) is propagated in the short-time regime ( $t$ -cube approximation). The energy deposited during this pulse is used to heat the atmosphere in the long-time approximation. If the second pulse follows the first pulse in a time large compared to the hydrodynamic time it will encounter just this gas density. The second pulse itself again is in the short-time regime. No dissipation mechanism (wind, slewing, or natural convection) is included between the two pulses. Infinite Gaussian beams are used.

A measure of the strength of the first pulse is the quantity

$$E_c = \alpha e^{-\alpha R} k^2 E_p (\text{J/cm}^3)$$

where  $E_p$  is the total energy in the pulse,  $\alpha$  the absorption coefficient,  $R$  the range, and  $k$  the propagation constant.

In Fig. 1-11, the irradiance distribution of the second pulse is shown as a function of radius for some values of the energy of the precursor  $E_p$ . The first pulse for these cases shows no or very small thermal blooming. The cases studied are for the following conditions: range  $R = 3 \text{ km}$ ; absorption coefficient  $\alpha = 10^{-6} \text{ cm}^{-1}$ ; wavelength  $\lambda_0 = 2\pi/k = 10.6 \mu\text{m}$ ; beam quality parameter  $\beta = 4$ ; transmitter diameter  $D = 1 \text{ m}$ , infinite Gaussian; and focal area  $A = 100 \text{ cm}^2$ . A truncated Gaussian with a beam quality 3 has the same focal area and therefore the same thermal blooming.

The second pulse shows large thermal blooming if the energy of the precursor is above 2 kJ, or (expressed in a more general way) if  $E_c$  is above 3000  $\text{J/cm}^2$ .

J. Herrmann

### c. Four-Dimensional Propagation Code

In the past our propagation codes have been limited to three dimensions: the CW code has three spatial dimensions, and the pulse codes, assuming circular symmetry, have two spatial dimensions plus time. But there are a number of problems which develop in time, but without circular symmetry. For instance, the propagation of a CW beam through a stagnant zone does not lead (under our hypotheses) to a steady state; and the propagation of a pulse through a turbulent medium does not have circular symmetry. Thus it is clear that a full four-dimensional code would have interesting applications.

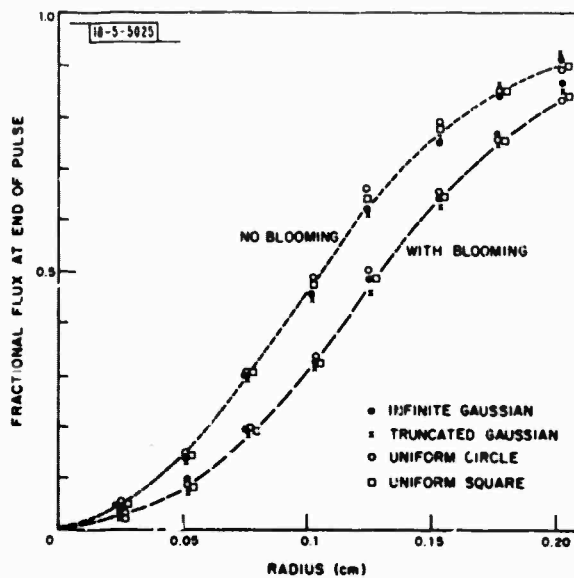


Fig. I-12. Flux within a circle of given radius in the focal plane, as a function of radius, for four initial irradiance distributions with and without blooming. Distributions at beginning of pulse, before blooming starts. Power -  $8 \times 10^6$  W; pulse length - 1  $\mu$ sec; absorption coefficient -  $1.5 \times 10^{-3}$  cm $^{-1}$ ; range - 4.9 m;  $\lambda = 15 \mu\text{m}$ ; and neck radius - 0.127 cm for all cases. Initial conditions for four cases: (a) side of square - 3.3 cm; (b) radius of uniform circle - 1.94 cm; (c) infinite Gaussian, 1/e power radius - 0.97 cm; (d) truncated Gaussian, 1/e power radius - 1.37 cm; radius of truncation - 1.94 cm.

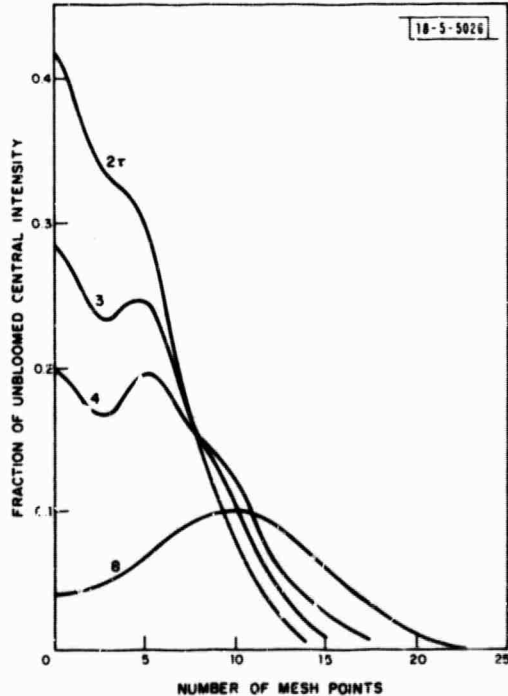


Fig. I-13. Time evolution of a modulated pulse (long-time approximation). Times in units of  $\tau$ , defined as  $\tau = \pi c_p T / 2 \alpha k^2 (n - 1) Pe^{-\alpha R}$ .

Unfortunately, a simple computation also makes it clear that a straightforward extension of our CW code into the time dimension by use of a standard hydrodynamic code would make prohibitive demands on both computer storage and computing time. We have, therefore, written a code that extends our CW code by a single time step, using either the short-time or the long-time approximation for the hydrodynamics. Experience with our circularly symmetric pulse codes has shown that these approximations are valid over a considerable range: the short-time approximation gives good results up to about half the hydrodynamic time, while the long-time approximation is reasonably good after 2 to 3 hydrodynamic times. Thus, it should be possible to cover a good fraction of the regimes of interest for pulse propagation using the new code. At present, this code does not include the capability of studying the stagnation zone problem, but an appropriate modification should not be difficult. The computing time and computer storage required in the code are nearly twice those for the corresponding CW computation.

Using this code we have compared the blooming for a uniformly illuminated square aperture with that for various circularly symmetric field distributions. The distributions were chosen so that the irradiance in the focal plane with no blooming averaged over angles was nearly the same for all of them (Fig. I-12). The conditions correspond to a laboratory case. When blooming was present (short-time approximation), the focal plane irradiance was again nearly the same (Fig. I-12), showing that the short-time blooming essentially depends only on the mean unbloomed behavior in the immediate vicinity of the focus.

L. C. Bradley  
J. Herrmann

#### d. Brueckner instabilities

Brueckner and Jorna<sup>5</sup> and Kroli and Kelley<sup>6</sup> have discussed the possible importance of dynamic instabilities as a limitation to the propagation of high-power laser beams. These arise from the coupling of the laser beam with entropy or sound waves, and are referred to as stimulated Rayleigh and Brillouin scattering, respectively. These analyses were linearized, and were principally concerned with infinite plane waves. Rangnekar<sup>7</sup> has made some numerical studies of instabilities in circularly symmetric collimated beams, using a ray-tracing technique. His results confirmed the order of magnitude of Brueckner's analytic formulas. In general one may say that for CW beams these effects are not likely to be important, because of the comparatively small irradiances involved and because of the smearing effect of convection. But for pulsed beams these considerations do not apply, and it is possible to get significant amplification of transverse intensity (or phase) fluctuation.

Recently indications of the presence of this effect have shown up in some of our pulse calculations. The observation is that numerical noise at the Nyquist frequency appears to be amplified in nonlinear propagation. In order to study this phenomenon, I have used our propagation code for pulses with initial conditions corresponding to various amplitude modulations of the initial beam. An example is shown in Fig. I-13 where the initial field consisted of a Gaussian plus a small admixture of a higher order eigenfunction of circular symmetry. To be specific, the field was taken to be proportional to

$$[1 + 0.05 L_{12}(r^2/a^2)] \exp(-r^2/2a^2)$$

Here  $L_n$  is the Laguerre polynomial of order  $n$ . It can be seen that, as time increases, the modulation first becomes stronger, and then largely disappears. In the present case the overall

effect of the modulation on the blooming is small, but it is not clear that this will be true for other conditions. In particular, it is possible that the effects of turbulence could be amplified by this mechanism. Further exploration is planned.

L. C. Bradley

#### e. Propagation of Second Pulse Through Fog and Aerosols

We can consider the effect of pulse beam spread due to a fog in a manner analogous to our discussion on CW beam spread due to aerosols cited previously (cf. Sec. I-A-1). However, for the pulse case the first pulse through the beam is greatly attenuated by scattering and water vapor absorption until the absorbed energy exceeds the threshold energy necessary for vaporization of all of the water

$$E > E_{\text{thres}} = h_v N_c \rho_w (\pi D^2 L / 4)$$

where  $h_v$  is the heat of vaporization,  $N_c$  is the number density of water droplets,  $D$  is the beam diameter,  $L$  is the path length through the fog, and  $\rho_w$  is the density of liquid water. Assuming the first pulse has sufficient energy to clear the fog, we then are interested in how well the next pulse (following by a few microseconds, for example, after the end of the previous pulse) is able to propagate through the cleared channel. The extinction coefficient of the water vapor is now considerably less than that of the water drops, and we can make a preliminary estimate of the beam spread due to multiple scattering. Because after a few microseconds the index spheres have expanded to a size much larger than the wavelength (cf. Sec. I-C-3), we may use the geometric optics approximation for multiple scattering through the ensemble of index spheres. As shown before for the CW case, the mean squared deflection is

$$y_r^2 = 4/9 L^3 N_r \pi a_r^2(t) (\Delta n/n)^2 .$$

For the pulsed case, we assume that the water droplet heats up to the critical temperature,  $T = 374^\circ\text{K}$ , and heat is then transferred rapidly to the air into a rapidly expanding heated air-vapor sphere. The composition of the vapor sphere is predominantly heated air whose velocity we have modelled empirically. We assume that the change in index of refraction is uniform throughout this index sphere and is then given by

$$\Delta n = \beta \Delta T \frac{r_w^3}{a^3(t)}$$

with

$$\beta = \alpha_g \frac{c_{pv} \rho_w}{c_{pa} T_0} = \frac{1}{600^\circ\text{K}}$$

and  $c_{pv,a}$  are the respective heats of the water vapor and air,  $\alpha_g$  is the Gladstone-Dale constant,  $\rho_w$  is the water density,  $T_0$  is the initial temperature,  $\Delta T \approx 350^\circ\text{K}$ ,  $r_w$  is the water droplet radius, and  $a(t)$  is the vapor sphere radius where  $t$  is measured approximately from the end of the first pulse. There is an additional concentric index sphere due to the initial vaporization shock which travels faster than Mach 1 and produces little effect for times of interest.

An appropriate distribution for fog radii is given by<sup>8</sup>

$$dN_r = N_0 \frac{r_w}{(r_m)^2} e^{-r_w/r_m} dr$$

where  $r_m$  is the peak of the distribution, so

$$y_{\text{total}} = \left[ \int_0^{\infty} y_r^2 dr \right]^{1/2} = \frac{2}{3} \frac{(7!)^{1/2} N_0^{1/2} \pi^{1/2} r_m^3 \beta \Delta T L^{3/2}}{a^2(t) n}$$

If we compare this with the corresponding diffraction-limited spreading for the pulsed case in fog, we have

$$\frac{y_{\text{total}}}{y_{\text{diff}}} \Big|_{\substack{\text{fog} \\ \text{pulsed beam}}} = \frac{2}{3} \frac{(7!)^{1/2} \pi^{1/2} L^{1/2} N_0^{1/2} r_m^3 \beta \Delta T D}{a^2(t) n \lambda}$$

For values of  $c_{pv} = 2 \text{ J/g}^\circ\text{K}$ ,  $c_{pa} = 1 \text{ J/g}^\circ\text{K}$ ,  $\rho_v = 1 \text{ g/cm}^3$ ,  $T_0 = 300^\circ\text{K}$ ,  $\alpha_g = 0.25 \text{ cm}^3/\text{g}$ ,  $L = 1 \text{ km}$ ,  $D = 2 \text{ cm}$ ,  $r_m = 0.6 \mu\text{m}$  (e.g., as measured by Harris<sup>9</sup>), and  $n = 1$ , we show in Fig. I-14 the development in time of the relative beam spread for three different fog droplet

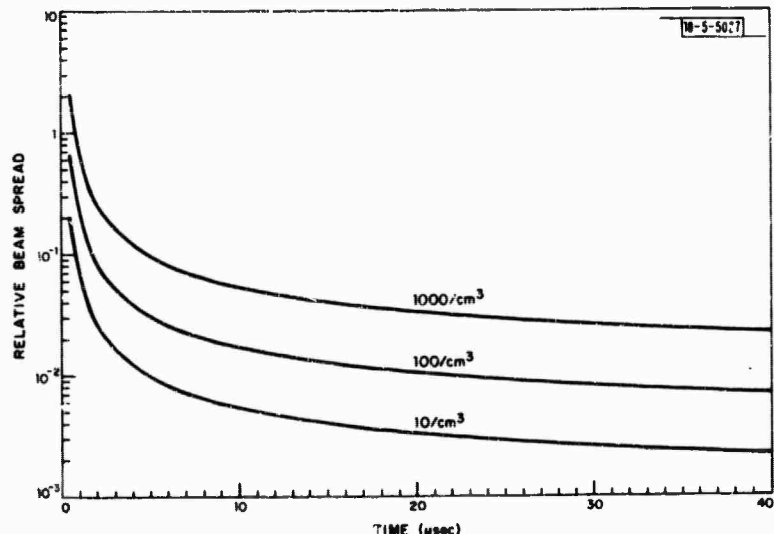


Fig. I-14. The rms total deflection normalized to the diffraction spread for a pulsed  $10.6-\mu\text{m}$  laser beam of uniform intensity and 2-cm diameter through a fog (with a peak in particle radius distribution of  $r_m = 0.6 \mu\text{m}$ ) of a path length of 1 km for three water droplet densities.

densities. A caution here is that fogs can range to distributions with a value of  $r_m$  as high as  $5 \mu\text{m}$  and since the deflections scales as  $r_m^3$ , the deflections can become considerably more severe than those indicated by Fig. I-14. The empirical value of  $a(t)$  described in Sec. I-C-3 of this report has been used.

TABLE I-1 COMPARISON OF PHYSICAL PARAMETERS OF CHIEF AEROSOL COMPONENTS					
	Boiling Point (°C)	Specific Gravity	$C_p$ (J/gm °K)	$\frac{c_p}{c_p \text{water}} \frac{\rho_{\text{aer}}}{\rho_w} \frac{\Delta T_{\text{aer}}}{\Delta T_w}$	
Carbon	4827	2.25	0.17(0.3)	1.9	
S:O <sub>2</sub>	2230	2.2	0.22	1.54	
NaCl	1413	2.16	0.21	0.91	

If we assume that in the pulse regime a heated aerosol acts very much like a water droplet, evaporating rapidly with a corresponding rapidly expanding sphere with approximately the same time evolution, we have for the relative rms beam spread

$$\left| \frac{y_{\text{total}}}{y_{\text{diff}}} \right|_{\substack{\text{aerosol} \\ \text{pulsed beam}}} = \frac{2}{3} \frac{\pi^{1/2} L^{1/2} N_0^{1/2} (r_{\max} r_{\min})^{3/2} \beta \Delta T D}{a^2(t) n \lambda}$$

where we have assumed again for aerosols the distribution  $l_r = 3r^{-4} N_0 r_{\min}^3 dr$  between radii of  $r_{\min}$  and  $r_{\max}$ . The rms deflection due to aerosols relative to that due to fogs for the same concentrations is then given by

$$\frac{y_{\text{aerosol}}}{y_{\text{fog}}} = \left[ \frac{(r_{\max} r_{\min})^{1/2}}{r_m} \right]^3 \frac{1}{(7!)^{1/2}} \frac{\Delta T_{\text{aer}} c_p \rho_{\text{aer}}}{\Delta T_{\text{wat}} c_p \rho_w}$$

In Table I-1 we list three of the dominant components of aerosols with their boiling points (hence approximate critical temperature change) and other relevant physical constants and compare the factor

$$\frac{c_p \rho_{\text{aer}} \Delta T_{\text{aer}}}{c_p \rho_w \Delta T_{\text{water}}} .$$

Multiplying the last column by 0.02 would give approximately the spread due to aerosols relative to a fog of the same concentration of scatterers. These results give us an initial indication of the significance of beam spread due to fogs and aerosols.

#### f. Propagation-Through-Fog Code

In order to solve a more accurate formulation of the beam spread of the second pulse through a cleared fog, we intend to modify the Bradley-Herrmann propagation code<sup>10</sup> to include the scattering effects due to the vapor spheres formed around the water droplets (or the index spheres that form around irradiated aerosol particles).

In the Bradley-Herrmann code, the effect of the medium is simulated by a phase change of the field propagated through a small axial increment. To employ the code we need to find if for

sufficiently low spatial frequencies the sum of scattered and incident field can be described accurately by a simple phase change, i.e., at each point in a plane of observation beyond the scatterers and perpendicular to the propagation direction of the incident beam,

$$E_{\text{inc}} + E_{\text{scatt}} \approx E_{\text{inc}} e^{ik_o \int n(z) dz},$$

where  $k_o$  is the optical wave number and  $n(z)$  is the index of refraction. For index changes not very large the exponential can be expanded to first order and the incident field terms subtracted

$$E_{\text{scatt}} = E_{\text{inc}} S(\Theta) \frac{\exp[(-R + z) ik_o]}{ik_o R} \approx E_{\text{inc}} ik_o \int n(z) dz.$$

We then wish to construct the given integrated index of refraction (or its corresponding spatial Fourier transform in the plane of observation) and check the validity of our low spatial frequency approximation.

The Fourier transform  $\nu(k)$  of the integrated phase change through the sphere is defined by

$$k_o \int n dz = \int \nu(k) e^{ik \cdot \vec{r}} d^2 k.$$

We wish to compare this with the Fourier transform of the scattered wave  $\nu'(k)$  defined by

$$-\frac{S_j(\Theta) \exp[(-R + z) ik_o]}{k_o R} = \int \nu'(k) e^{ik \cdot \vec{r}} d^2 k.$$

The geometry of this equation is shown in Fig. I-15 where  $\vec{R}$  is the vector from the center of the scatterer to a point of observation in the plane perpendicular to the incident direction,  $\vec{z}$  is the vector along the incident direction from the scatterer to the incident plane,  $k_o$  is the optical wave

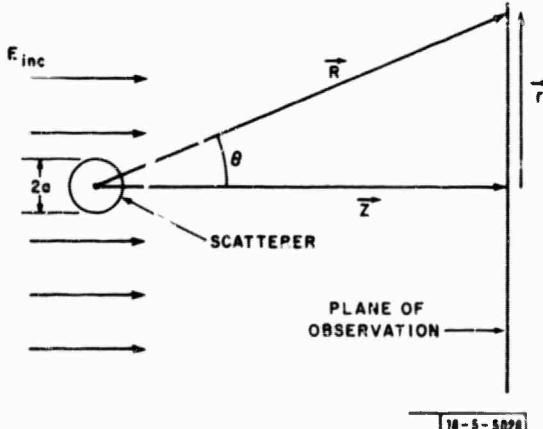


Fig. I-15. View of the geometry of scattered radiation problem for a single fog droplet.

number, and  $S_j(\Theta)$  are the scattering amplitude functions for the perpendicular and parallel electric field components as a function of the angle  $\theta$  between  $\vec{z}$  and  $\vec{R}$ . Also,  $\vec{k}$  is the spatial wave vector in the plane of observation and  $\vec{r}$  is the vector from the intercept of  $\vec{z}$  and the plane to the point of observation in the plane. The spatial transform for a single particle is then given by

$$\nu'(k) = \frac{1}{2\pi} \int_0^\infty dr r J_0(kr) \frac{\cos \theta S_j(\Theta) \exp[(-\frac{z}{\cos \theta} + z) ik_o]}{k_o z}. \quad (I-4)$$

For times greater than a few microseconds, the vapor spheres become much larger than the wavelength of the incident light, and the total scattering component from a single sphere is much less than the incident field on the sphere, so it is appropriate to employ the Rayleigh-Gans approximation for the scattered field<sup>11</sup>

$$S_j(\theta) = ik_o^3 a^3 \Delta n \frac{(2\pi)^{1/2}}{(2k_o a \sin 1/2 \theta)^{3/2}} J_{3/2}(2k_o a \sin 1/2 \theta) \begin{cases} 1 \\ \cos \theta \end{cases} . \quad (1-2)$$

In Eq. (1-2) the respective upper and lower scattering amplitudes are for electric field components perpendicular and parallel to the reference plane, and  $\Delta n$  is the uniform index change within a sphere of radius  $a$  which is expanding in time. By using trigonometric identities and variable substitutions, we can rewrite (1-1) as

$$\nu'(k) = \frac{2k_o^2 a^3 \Delta n}{2^{1/4} (k_o a)^{3/2} \pi^{1/2} i} \times \left[ \int_0^\infty ds J_0(\sqrt{2} k z s) J_{3/2}(\sqrt{2} k_o a s) \right. \\ \left. \times s^{-1/2} \exp[-(ik_o z s^2 + bs^2)] \right] \quad (1-3)$$

where we have assumed that  $s \ll 1$  (the approximations involved are within 50 percent accuracy even for  $\theta = \pi/3$  or  $s = 1$ ) and introduced the expression  $\exp(-bs^2)$  to limit contributions for large  $s$  (i.e.,  $b$  must be at least comparable to 1). The introduction of the exponential limits contributions from the integral for large  $s$  which only occur as a result of our approximations, thus allowing the integral to converge. Additionally, only the small-angle scatter contributions interest us since large-angle scatter produces an effective attenuation. The integral (1-3) can be done exactly and the result is:

$$\nu'(k) = \frac{k_o^2 a^3 \Delta n}{3\pi i} \frac{z}{ik_o z + b} \sum_{m=0}^{\infty} (-1)^m \left[ \frac{k^2 z^2}{2(ikz + b)} \right] \frac{1}{m!} F\left(-m, -m; 5/2; \frac{k_o^2 a^2}{k^2 z^2}\right) \quad (1-4)$$

where  $F$  is the hypergeometric function,

$$\alpha = \frac{k^2 z^2}{2(ik_o z + b)} \quad \text{and} \quad u = \frac{k_o^2 a^2}{k^2 z^2} .$$

For large values of  $z$  and for values of  $a$  not too large, both  $u$  and  $\alpha u$  will be much less than 1, and we can curtail the expansion to the leading terms in  $u$  and retain terms only to second order in  $\alpha$ . We then need for our analysis the spatial spectrum  $\langle \nu'(k) \nu'^*(k) \rangle$ , which is averaged over  $z$  since the axial position of the particle is a random variable. Retaining terms only to fourth order in  $k$  we find

$$\langle \nu'(k) \nu'^*(k) \rangle = \frac{k_o^2 a^6 \Delta n^2}{9\pi^2} \left[ 1 - \frac{k^2}{k_o^2} b + \frac{k^4 b^2}{2k_o^2} - \dots \right] . \quad (1-5)$$

If we compare this to the corresponding geometric optics solution for light passing through a uniform sphere, we find the spatial spectrum to be

$$\langle \nu(k) \nu^*(k) \rangle = \frac{k^2 a^6 \Delta n^2}{9\pi^2} \left[ 1 - \frac{1}{5} (ka)^2 + \frac{19}{1400} (ka)^4 - \dots \right] .$$

The agreement to first order allows us to use (1-5) in place of (1-4) in our propagation code.

We next must incorporate the single-particle spectrum into the spectrum of a density of randomly distributed such particles, and we shall then be able to begin our computer simulation of the distortion of the second pulse through an evaporated fog channel. Our initial assumptions for the multiparticle system are that the position of the particles are uncorrelated, which yields the almost white noise spectrum. However, we anticipate that we shall eventually require correlation of particle position to account, for example, for tufts of fog.

H. Granek  
L. C. Bradley

#### f. Propagation of a Focused Beam Through an Absorbing Medium

This section considers the extent to which the atmosphere  $\text{CO}_2$  can be described as a saturable medium to  $10.6\text{-}\mu\text{m}$  radiation with a phenomenological absorption coefficient given by

$$\alpha = \alpha_0 / (1 + I/I_s)$$

For a simple two-level system of the type described by Selden<sup>12</sup> (Fig. 1-16), the interaction with radiation will cause a transient change in level populations followed by a steady-state absorption. The time-dependent coupled equations describing such a simple system are

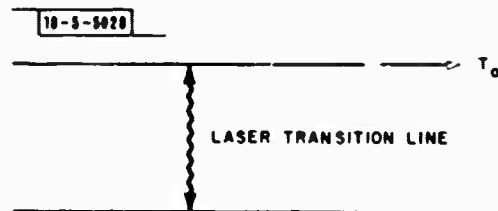
$$\frac{dI}{dz} = -\sigma I(n_2 - n_1)$$

$$\frac{dn_2}{dt} = -\frac{\sigma I}{h\nu}(n_2 - n_1) - n_2/T_0$$

$$\frac{dn_1}{dt} = +\frac{\sigma I}{h\nu}(n_2 - n_1) + n_2/T_0$$

Here,  $I$  = intensity,  $n_2$  = density of the upper level,  $n_1$  = density of the lower level,  $\sigma$  = absorption cross section, and  $T_0$  is the relaxation rate of the upper level.

Fig. 1-16. Illustrated is a simple two-level system which absorbs laser radiation.



After the initial transient radiation edge, a steady state will evolve which is governed by the incident intensity and the effectiveness of the relaxation of the upper level with relaxation time  $T_0$ . In such a steady state the temporal rates of change of the populations are zero. By substituting the second rate equation into the first, the rate of change of the intensity is given in terms of the upper level only. Now using the second equation and the condition that the total population of both levels is some constant value  $n$ , the following equation results:

$$\frac{dI}{dz} = \frac{-\sigma n I}{(1 + I/I_s)}$$

where

$$I_s = \frac{h\nu}{2\sigma T_0}$$

10-5-5830

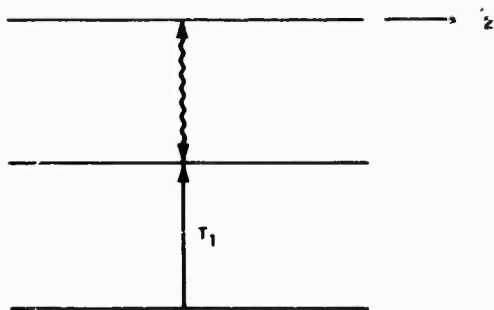


Fig. I-17. Illustrated is a three-level system which approximates absorption in the atmosphere by CO<sub>2</sub>.

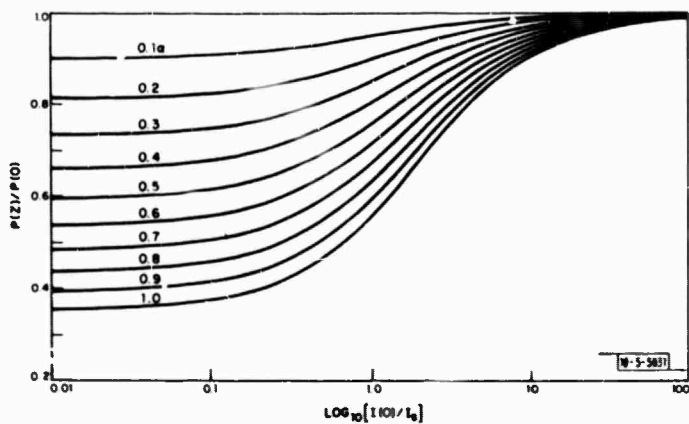


Fig. I-18. The graph of  $P(Z)/P(0)$  versus  $I(0)/I_s$  with  $A_{in} = 10^2$  cm,  $A_{out} = 0.1$  cm,  $f = 490$  cm, and  $\alpha = 2 \times 10^{-3}$ .

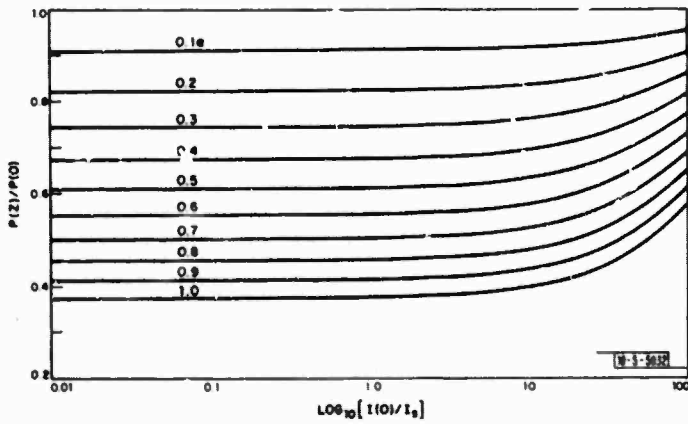


Fig. I-19. A plot of  $P(Z)/P(0)$  versus  $I(0)/I_s$  with  $A_{in} = 10^4$ ,  $A_{out} = 10^2$ ,  $f = 10^5$  cm, and  $\alpha = 10^{-5}$ .

Considering a three-level system, illustrated in Fig. I-17, the same procedure will result in the following expression:

$$\frac{dI}{dZ} = \frac{-\sigma nl}{2(1 + 1/I_s)}$$

where now

$$I_s = \frac{2h\nu}{(3T_2 + T_1)\sigma}$$

Here  $T_1$  is the relaxation rate for the second level to the first, and  $T_2$  is the relaxation rate of the third level to the first by collisions.

For the propagation of 10.6-μm radiation through the atmosphere, this simple three-level system will be used to estimate the saturation intensity.<sup>2</sup> The upper laser level in CO<sub>2</sub> is quickly relaxed by N<sub>2</sub> which remains excited for the duration of the pulse. The rate at which the lower laser level is populated depends on T-V collisional excitation of the lowest vibrational level. Water vapor contributes heavily to this process and  $T_1$  is given by

$$\frac{1}{T_1} = \frac{1}{T_{H_2O}} + \frac{1}{T_R}$$

where  $T_R$  is due to other molecules.

For a focused beam, the usual phenomenological expression for the rate of change of intensity with distance must be modified to account for the increase in the intensity due to a fixed power being concentrated over a progressively smaller area. This gives an additional term as shown below

$$\frac{dI}{dZ} + \frac{\partial A}{\partial Z} \frac{I}{A} = \frac{-\alpha I}{(1 + I/I_s)}$$

By redefining  $I = \gamma I_s A_0 / A(Z)$  and letting  $Z\alpha = \rho$ , the equation achieves the compact form

$$\frac{\partial \gamma}{\partial \rho} = \frac{-\gamma}{1 + \frac{\gamma A_0}{A(Z)}}$$

This yields the following formal solution

$$\gamma = \gamma(0) \exp \left[ - \int_0^\rho \frac{d\rho'}{1 + \frac{\gamma A_0}{A(\rho')}} \right]$$

Thus, the value of  $\gamma$  at  $\rho$  is related at  $\rho + \delta\rho$  by the approximate relation

$$\gamma(\rho + \delta\rho) \approx \gamma(\rho) \exp \left\{ -\delta\rho / \frac{[1 + \gamma(\rho) A_0]}{A(\rho)} \right\}$$

By using this simple iteration, a numerical evaluation of  $P(Z)/P(0) = \gamma(\alpha Z)/\gamma(0)$  is extremely efficient resulting in values of the type shown in Figs. I-18 to I-20. These figures are representative of a laboratory situation (a 10-cm beam focused to a 3-mm spot in 5 meters) and two field situations (a 1-meter-diameter beam focused to a 10-cm spot over 1 km and a collimated 10-cm-diameter beam).

D. L. Mooney J. E. Lowder  
H. Kleiman R. W. O'Neil

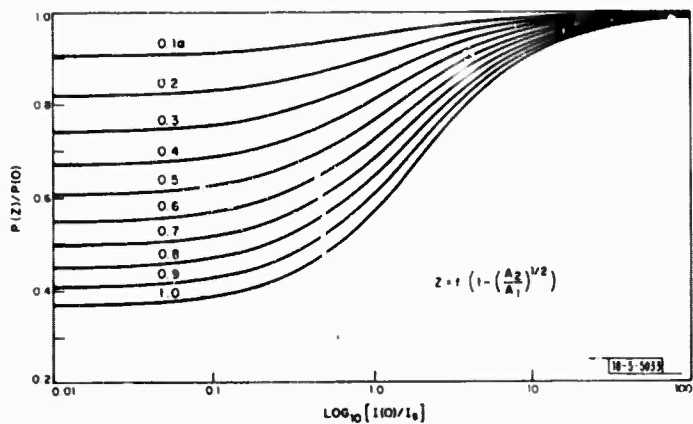


Fig. I-20. The graph of  $P(z)/P(0)$  with constant area of  $10^2 \text{ cm}^2$  and  $\alpha = 2 \times 10^{-3}$ .

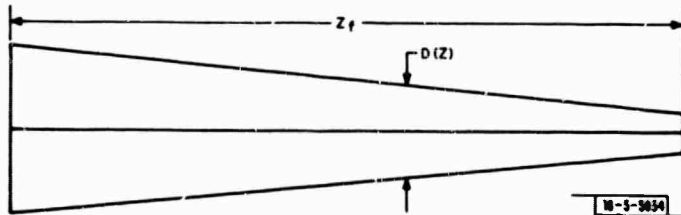


Fig. I-21. Geometry for saturation calculations.

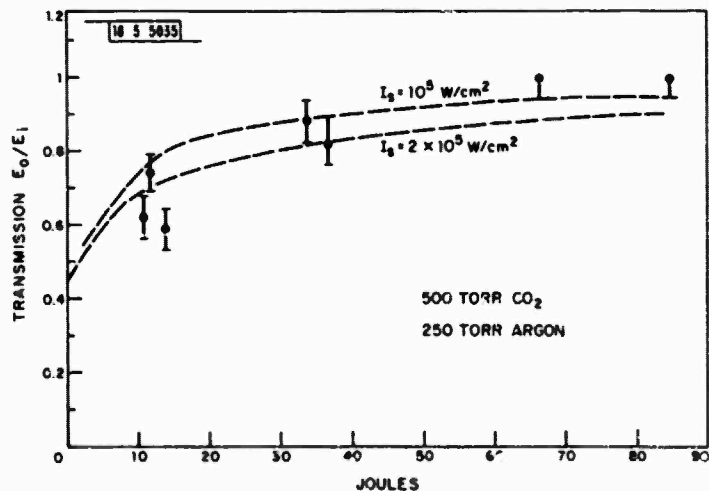


Fig. I-22. Plot of ratio of the incident power to the transmitted power as a function of the ratio of the transmitted intensity to the saturation intensity.

## 2. Experiments

### a. Pulsed Thermal Blooming and Saturation of CO<sub>2</sub> at 10.6 μm

The experiments described in the previous Optics Research Report<sup>3</sup> have been analyzed. The results for absorption by a broadband absorber (propane) causing thermal blooming within a hydrodynamic time have been submitted for publication.<sup>13</sup>

A number of experiments were also done in which the primary absorber was 500 torrs CO<sub>2</sub> in 250 torrs argon. The primary physical process we were interested in examining here was the saturation of the CO<sub>2</sub>. For pulse lengths of the type used (~10 μsec) it is justified to use steady-state kinetics in describing the saturation. Hence, we describe the absorption coefficient phenomenologically by:

$$\alpha = \alpha_0 / i + (i / i_s)$$

Here,  $\alpha_0$  is the linear absorption coefficient.

Then using the geometry shown in Fig. I-21

$$\frac{dP}{dZ} = \alpha P = \frac{\alpha_0 P}{1 + \frac{\pi}{4} D^2(Z) i_s}$$

where

$$D(Z) = \lambda \left[ \frac{Z_f^2/4 + 4Z^2}{Z_f/2} \right]^{1/2}$$

Here, P = power, λ = wavelength, Z<sub>f</sub> the focal length, Z the distance as measured from the focal point, and i<sub>s</sub> the saturation intensity.

One can solve this differential equation numerically. If one solves for P(Z), then P(Z = 0)/P(Z = Z<sub>f</sub>) is the fraction of the power transmitted through the absorbing cell. Using i<sub>s</sub> as an adjustable parameter we have fit curves of this type to the data as shown in Fig. I-22. For the conditions of our experiment ( $\alpha = 1.8 \times 10^{-3} \text{ cm}^{-1}$ , Z<sub>f</sub> = 490 cm), we obtain i<sub>s</sub> = 1 to  $2 \times 10^5 \text{ W/cm}^2$ .

We are currently working on more sophisticated theory detailed in Sec. II-A-4 to explain the magnitude of the saturation parameter.

H. Kleiman  
R. W. O'Neil  
J. E. Lowder

### b. Laser-induced Air Breakdown for 1.06-μm Radiation

Experiments have been done at 1.06 μm for the breakdown threshold in clean air and in carbon aerosol as a function of spot size. A Q-switched neodymium glass laser providing 6 J in a 100-nsec pulse was used for these experiments.

The breakdown threshold (50 percent probability of breakdown) in clean air was measured in a chamber with highly filtered air for four spot sizes. The spot size of  $10^{-2} \text{ cm}$  was the largest value for which clean air breakdown could be obtained (on ~10 percent of the shots) with the available pulse power. The difference between the laboratory air threshold and the clean air value was observable only for the largest spot where the laboratory air threshold was ~0.5 that in clean air. The data are shown in Fig. I-23.

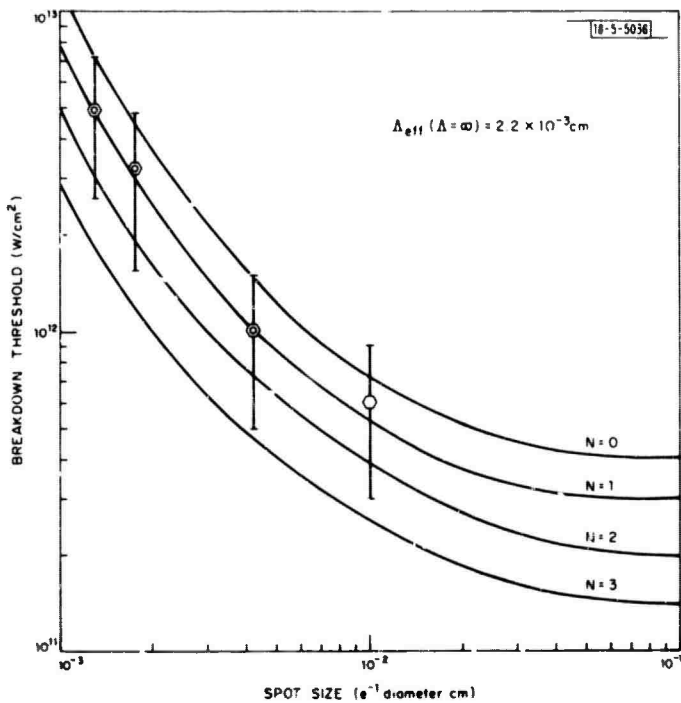


Fig. I-23. Breakdown threshold in clean air as a function of spot size. Solid curves are from Ref. 17 with  $\Lambda = D/7$  and  $\tau_p = 100$  nsec. The error bars indicate threshold uncertainty. The relative accuracy is  $\approx \pm 20$  percent.

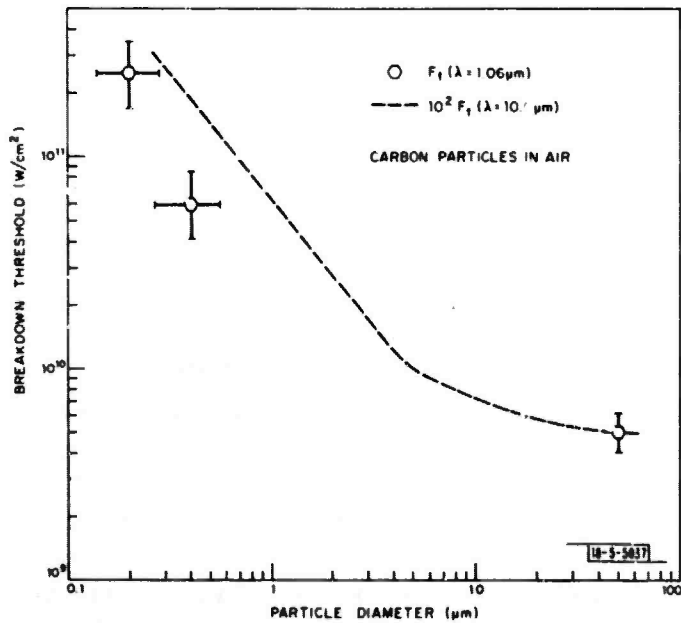


Fig. I-24. Threshold in carbon aerosol as a function of particle size. The value at 50  $\mu\text{m}$  was measured for single particles in a 270- $\mu\text{m}$  spot. The values for smaller particles were obtained for a 100- $\mu\text{m}$  spot in a carbon dust atmosphere where the particle size indicates the estimated value for the largest particle in the focal volume. The relative accuracies for the thresholds are  $\pm 20$  percent.

The results for clean air indicate somewhat higher thresholds than have been reported previously.<sup>14-16</sup> There are several factors which can account for this. For small spot sizes the threshold is very sensitive to diffusion length which depends on the intensity distribution in the focused spot, while for larger spots the threshold can be lowered by the presence of naturally occurring laboratory dust<sup>17</sup> as will be discussed below.

The solid curves in Fig. I-23 are theoretical values obtained from Ref. 18 for  $\tau_p = 100$  nsec and a diffusion length  $A = D/7$ . The different curves correspond to the inclusion in their calculations of various photoelectric processes requiring  $n$  or fewer photons.  $n = 0$  corresponds to the classical microwave theory.

These results suggest that one and possibly two photon processes are involved in 1.06- $\mu\text{m}$  breakdown but the dominant mechanism appears to be cascade ionization. The  $x^{-2}$  scaling of microwave theory, which is valid at 10.6  $\mu\text{m}$  (Ref. 17), is just becoming invalid at 1.06  $\mu\text{m}$ . A similar conclusion was arrived at from experiments involving 1.06  $\mu\text{m}$  and shorter wavelengths.<sup>16,19</sup>

The effects of particles on the threshold were investigated using the techniques described in Refs. 17 and 20. Single, 50- $\mu\text{m}$  carbon particles were positioned at the center of a 270- $\mu\text{m}$  focused spot. The threshold for this case was  $\approx 5 \times 10^9$  W/cm<sup>2</sup> or  $\approx 0.02$  of the clean air threshold. The threshold was then measured in a carbon aerosol for a 100- $\mu\text{m}$  spot. The measured values for light and heavy dust conditions were, respectively,  $\approx 2.5 \times 10^{11}$  and  $6 \times 10^{10}$  W/cm<sup>2</sup>. The dust content in the beam can be characterized by the size of the largest particle in a focal volume. The threshold data are shown in Fig. I-24 for the corresponding particle size. The dashed curve represents  $10^2$  times the similar threshold measured at 10.6  $\mu\text{m}$  (Ref. 17). The thresholds measured for the 100- $\mu\text{m}$  spot in a dust environment can be compared directly with the corresponding clean air threshold shown in Fig. I-23: these being from 0.1 to 0.4 times the clean air value. It should be noted that the values in the dusty air are comparable to the previously reported thresholds in air.<sup>14-16</sup>

The primary conclusions from this paper are that (1) cascade ionization is the dominant breakdown mechanism at 1.06  $\mu\text{m}$  with contributions from one- and two-photon processes, (2) threshold measurements in air for spot sizes larger than  $\approx 10^{-2}$  cm can be lowered by the presence of laboratory dust, and (3) the fractional reduction is comparable to those observed at 10.6  $\mu\text{m}$ .

D. E. Lencioni

### c. Dynamics of Particle-Induced Air Breakdown in A Laser Beam

Further experiments<sup>20</sup> on air breakdown triggered by single 50- $\mu\text{m}$  carbon particles were done to study the growth dynamics of the breakdown within the laser beam as a function of laser intensity, and the absorption length in the breakdown plasma.<sup>21</sup>

The experimental apparatus is shown in Fig. I-25. The laser beam was provided by a 5 J per pulse Febetron-CO<sub>2</sub> laser operated in the short-pulse mode.<sup>22</sup> An image converter camera, with exposure times down to 10 nsec, was used to obtain time-resolved information on the growth of the breakdown in the beam. The transmitted beam was reimaged and magnified 9:1 at a pair of photon drag detectors to obtain the radial and temporal dependence of the transmitted beam.

Figure I-26 shows a series of image converter frames which illustrate the growth of a breakdown at near threshold intensity. The dashed white lines mark the  $e^{-1}$  diameter of the beam which was 1 mm. The laser beam was incident from the left. The four frames were taken on four separate shots at the indicated exposure times relative to the start of the pulse. The

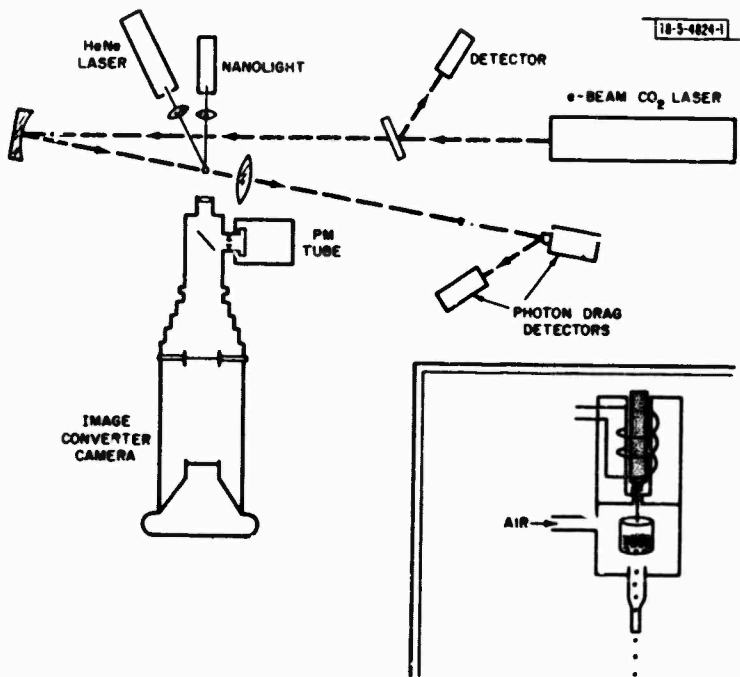


**Fig. I-25.** Experimental apparatus to study breakdown dynamics. Time-resolved information on the growth dynamics was obtained with the image converter camera. Particles were placed at a spot in the focal volume with the activated particle dropper shown in the insert.

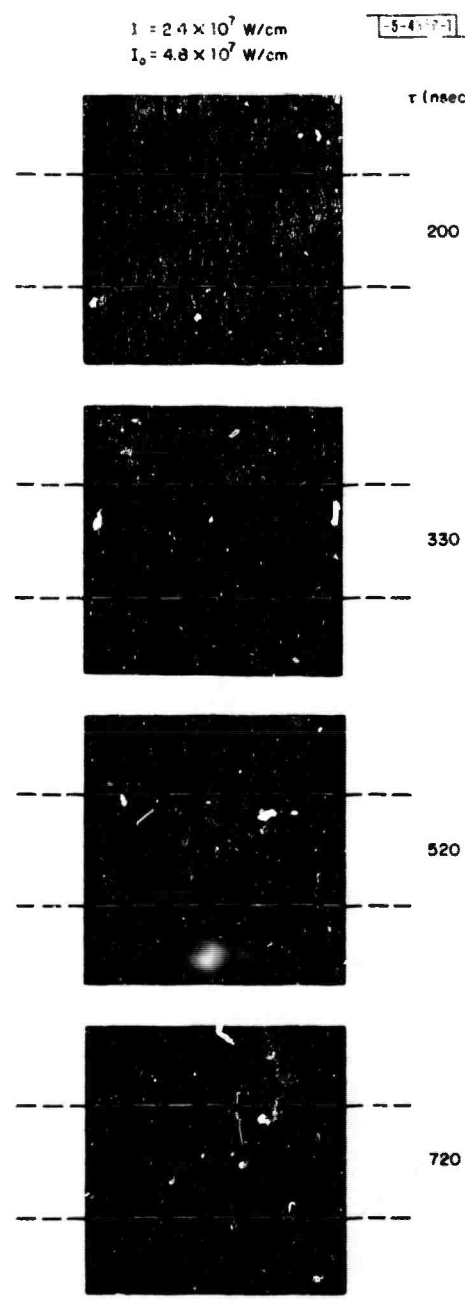


Fig. I-26. Series of image converter frames illustrating breakdown growth at near-threshold intensity.

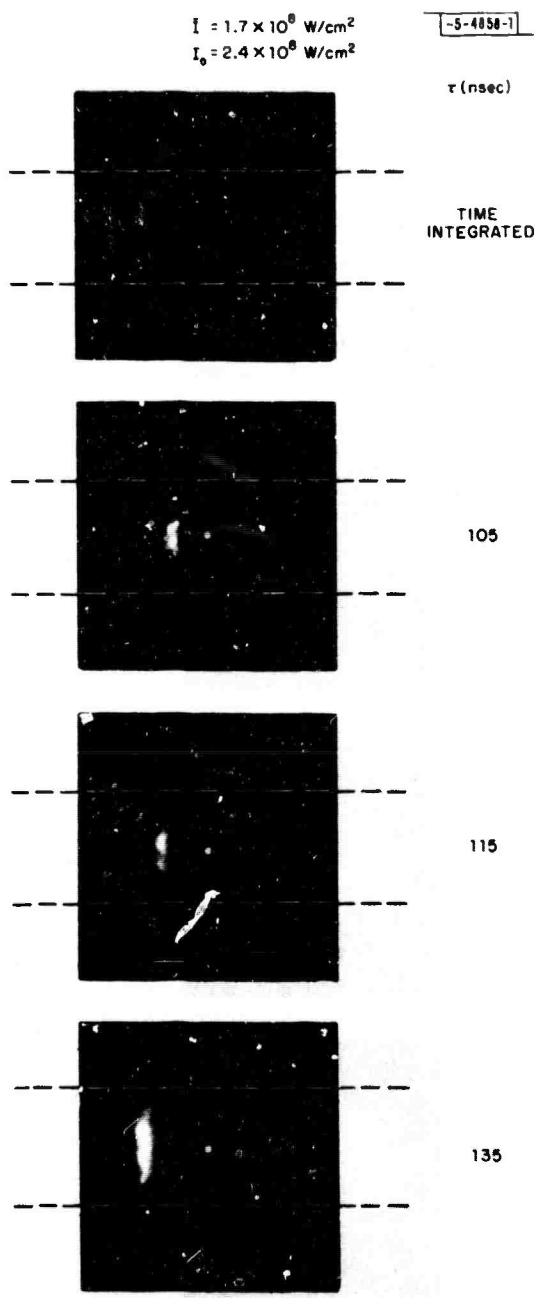


Fig. I-27. Breakdown dynamics at five times threshold intensity.

breakdown initiates at near the peak laser intensity and grows radially and axially as a volume absorbing plasma. The axial velocity is slightly larger than the radial velocity which had an initial value  $\approx 1.4 \times 10^5$  cm/sec. The velocities were observed to decrease by  $\approx 25$  percent after  $\approx 300 \mu\text{sec}$  due probably to the natural decay in laser intensity. Note that the particle remains visible in each of the frames.

At higher laser intensities the character of the breakdown growth changed abruptly. This is illustrated in Fig. I-27 where the intensity was increased above threshold by a factor of 5. In these frames a white dot has been inserted to indicate the position of the particle. Note that for these higher intensities the breakdown develops as a thin absorbing front which propagates back towards the laser and grows radially. Note also the increase in velocities. This type of breakdown growth is characteristic of the LSD described by Raizer.<sup>23</sup>

The radial and axial velocities obtained from data of this type are shown in Fig. I-28 as a function of intensity. At lower intensities the velocities increase rapidly with intensity roughly proportional to 1. At higher intensities the axial velocity varies roughly as  $I^{1/3}$ , which is in agreement with planar LSD wave theory.

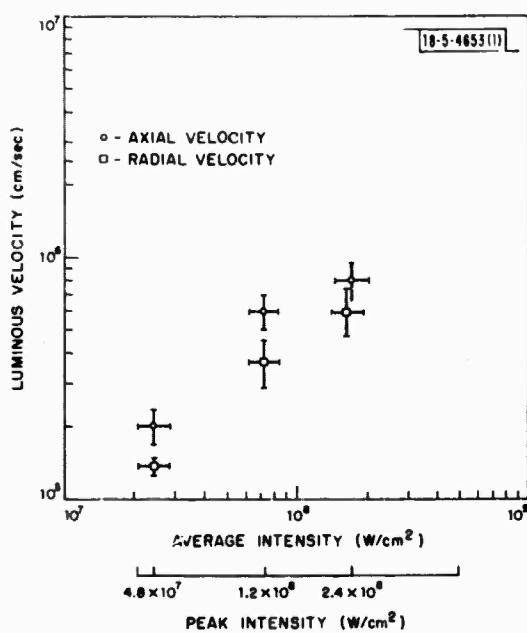


Fig. I-28. Axial and radial velocities of breakdown plasma.

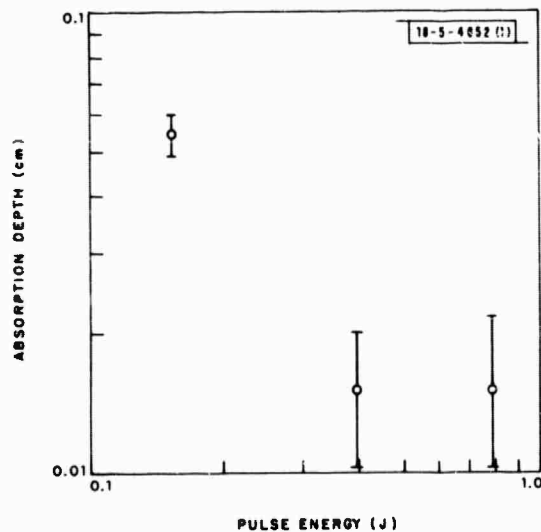


Fig. I-29. Absorption depth in breakdown plasma.

The absorption of laser intensity within the breakdown for a spot diameter of 1 mm was measured directly by reimaging the focal spot with magnification on two photon drag detectors: one giving the power transmitted through the central disk of radius  $r = 0.028$  cm and the other giving the power through a concentric annulus with inner radius  $r_1$  and outer radius 0.067 cm. The absorption depth within the breakdown was estimated by comparing the luminous thickness with the transmitted intensity. The results are shown in Fig. I-29.

D. E. Lencioni  
L. C. Pettingill

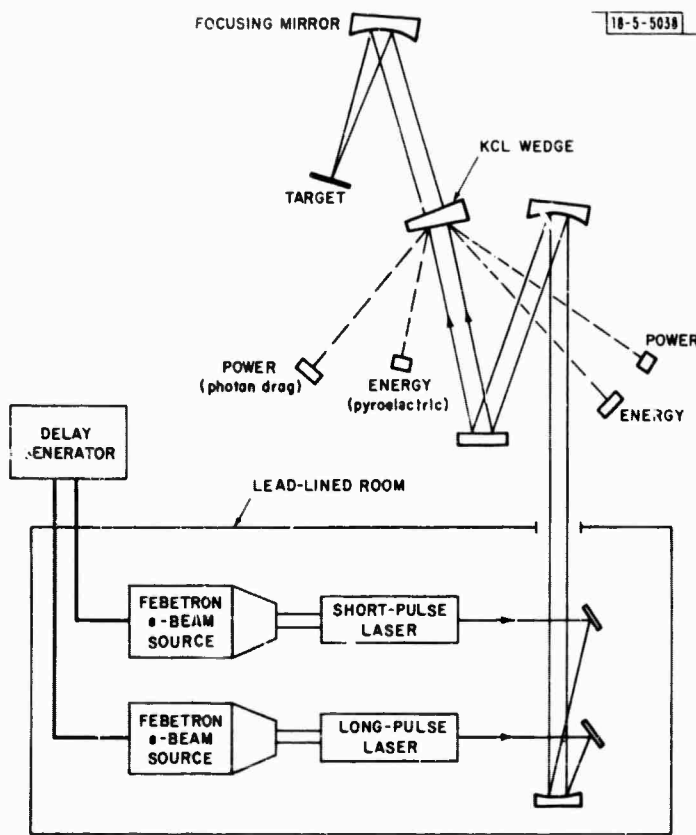


Fig. I-30. Experimental arrangement of double-pulse Febetron-CO<sub>2</sub> laser system. Power and energy of each beam are monitored with photon drag and pyroelectric (BaTiO<sub>3</sub>) detectors. The trigger system is connected to delay generators to provide a continuously adjustable delay between the laser firings.

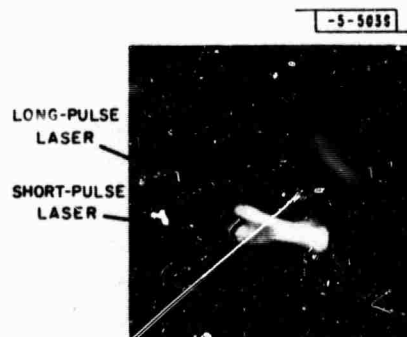


Fig. I-31. Open-shutter photograph of the plasma pattern created by a double-pulse shot on an aluminum target.

### C. EFFECTS

#### 1. Double-Pulse Pressure and Impulse Measurements

Measurements of surface pressure and impulse delivered to aluminum and carbon targets are reported in which two laser pulses spaced by a variable time delay were used. The measurements are presented in a normalized form to show the effect of the first pulse on the peak pressure and impulse delivered by the second pulse.

The experimental arrangement is shown in Fig. I-30. The two CO<sub>2</sub> e-beam lasers are described in Refs. 24 and 22 and were mounted in a lead-lined room as indicated in Fig. I-30. The 3-cm-diameter laser beams were made parallel with about a 1-cm separation between them and propagated through the optical system shown in Fig. I-30. The two beams were focused onto the same spot at the target surface with either a 15-cm or a 28-cm focal length mirror. The effect of the convergence angle of the two beams is shown in an open-shutter photograph of the two laser-produced plasmas in Fig. I-31. One laser was operated in the long-pulse mode<sup>24</sup> with an energy of about 10 J and a pulse length which varied from 40 to 50  $\mu$ sec. The second laser was operated in the TEA-pulse mode<sup>22</sup> with an energy of about 7 J and a pulse length of from 2 to 3  $\mu$ sec. Typical pulse shapes for these two lasers are shown in Fig. I-32. The focal spot sizes

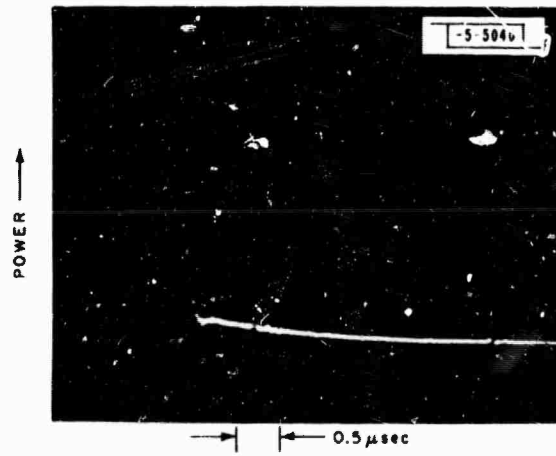
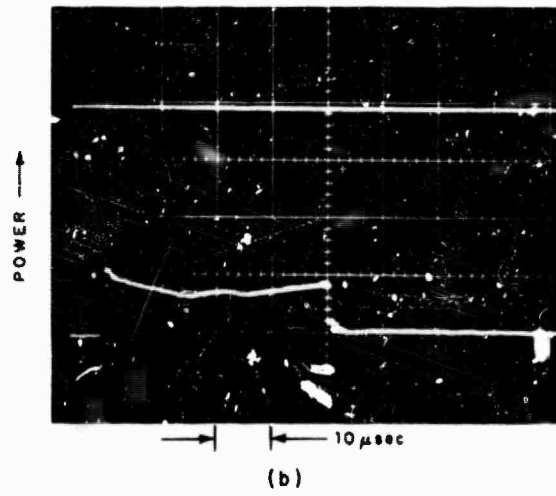


Fig. I-32. Typical pulse shapes of (a) short-pulse laser, (b) long-pulse laser measured with photon drag detectors.



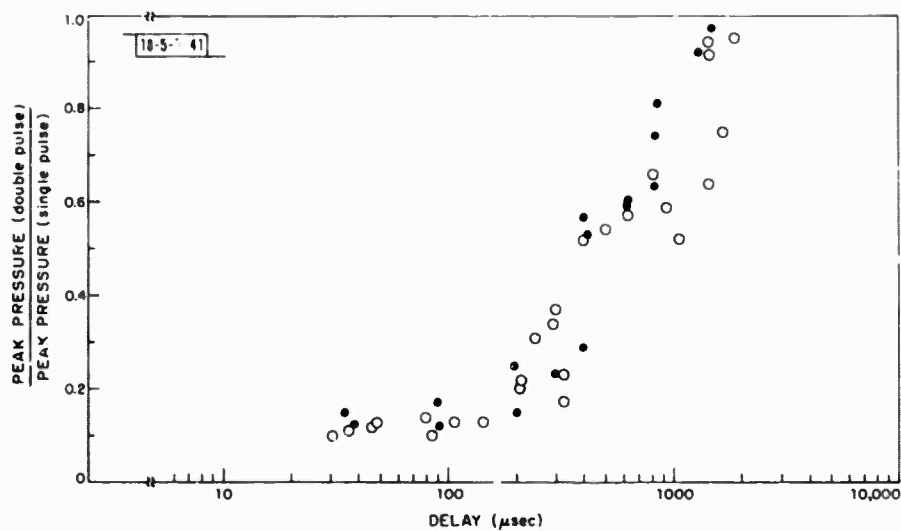


Fig. I-33. Peak pressure on an aluminum surface due to irradiation by short pulse after long-pulse precursor normalized by the peak pressure due to the short pulse in the absence of a precursor. The open symbols indicate second-pulse peak power densities of about  $7 \times 10^8 \text{ W/cm}^2$  and the solid symbols indicate power densities of about  $2 \times 10^8 \text{ W/cm}^2$ .

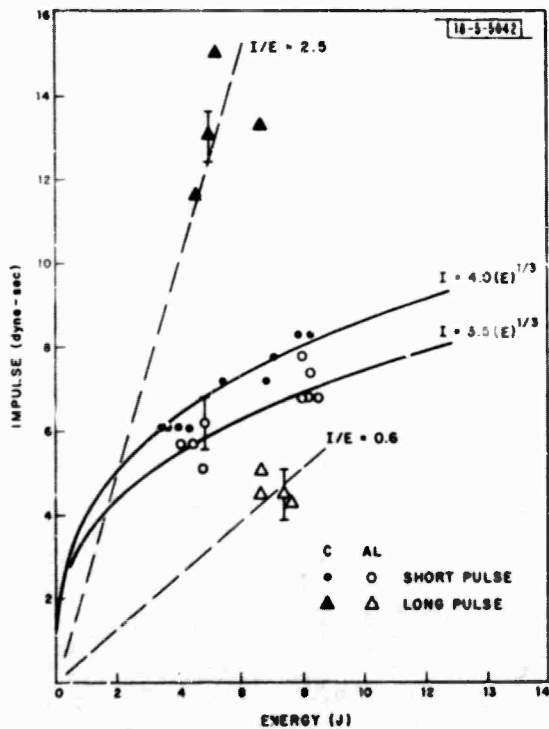


Fig. I-34. Impulse delivered to 0.38-cm-diameter aluminum and carbon targets as a function of incident single-pulse energy. The error bars denote the estimated maximum error of the impulse measurement.

used in obtaining peak power densities were obtained by attenuating the incident beam with fine perforated screens and observing the variation of the resulting burn areas on thermally sensitive paper.<sup>25</sup> Peak power densities incident on the target were a few  $\times 10^6$  W/cm<sup>2</sup> for the long-pulse laser and a few  $\times 10^8$  W/cm<sup>2</sup> for the short-pulse laser.

Relative peak pressure measurements in the focal spot were made with a PCB/Piezotronics quartz pressure gauge which was covered with a 1-mil sheet of pure aluminum. The thin aluminum sheet was attached to the 0.38-cm-diameter diaphragm of the quartz gauge with a thin layer of silicone grease. The peak pressure was measured first for the short pulse alone, then the pressure resulting from the short pulse preceded by the long pulse was measured for various delay times. The measured single-pulse peak pressures ranged from about 10 bar for the long-pulse laser to about 40 bar for the short-pulse laser. These measurements are lower limits to the actual peak pressures at the target surface due to the 1-μsec response time of the pressure gauges, but the measurements do provide a good relative measure of the actual single- and double-pulse target pressures. The normalized peak pressure measurements for the short pulse preceded by the long pulse are shown in Fig. 1-33 as a function of delay time. These results show the peak pressure caused by the short-pulse laser is reduced to about 10 percent of its normal value right after the long-pulse precursor, and it takes a delay of the firing time of the short pulse of from 1 to 2 msec for the peak pressure to recover to its single-pulse value.

The impulse delivered to 0.38-cm-diameter aluminum and carbon targets was measured with a sensitive ballistic pendulum. The impulse was found from the mass of the pendulum and the maximum amplitude of its swing which was measured with a photodiode-light source assembly. The pendulum was calibrated both by measuring the period to determine its effective length and by impacting it with small bodies of known momentum. The single-pulse impulse measurements for both the long- and short-pulse lasers are shown in Fig. 1-34. The impulse delivered by the short-pulse laser was found to vary roughly as the cube root of the incident energy with a little more impulse being delivered to carbon targets. For a fixed pulse shape and focal spot size, the peak power density incident on the target is proportional to the energy in the pulse. Thus, the energy dependence shown in Fig. 1-34 is in agreement with results presented in Refs. 26, 27, and 28 which show the impulse delivered to small targets is proportional to

$$I \propto A_T D_S(q)^{1/3}$$

where  $A_T$  is the target area,  $D_S$  is the focal spot diameter, and  $q$  is the incident power density. The impulse delivered by the long-pulse laser was found to be much higher for carbon than for aluminum targets as is shown in Fig. 1-34. The impulse delivered by the long-pulse laser was strongly influenced by blowoff, and since carbon has a much higher surface absorptivity ( $\alpha \approx 85$  percent)<sup>29</sup> for 10.6-μm radiation than aluminum ( $\alpha \approx 3$  percent),<sup>29</sup> the impulse was correspondingly greater. The relationship between impulse and energy for each set of data shown in Fig. 1-34 was used to determine the impulse delivered for the case of each pulse alone. The lasers were then fired in the double-pulse mode, with the long-pulse laser as the precursor, and the total impulse transferred to aluminum and carbon targets was measured as a function of delay time. The results are presented in Fig. 1-35 where the total impulse measured in the double-pulse mode is normalized by the sum of the impulses which would have been delivered if each laser had been fired separately. The results in Fig. 1-35 show the total impulse delivered to the targets varies from 50 to 80 percent of the value to be expected for single firings. The

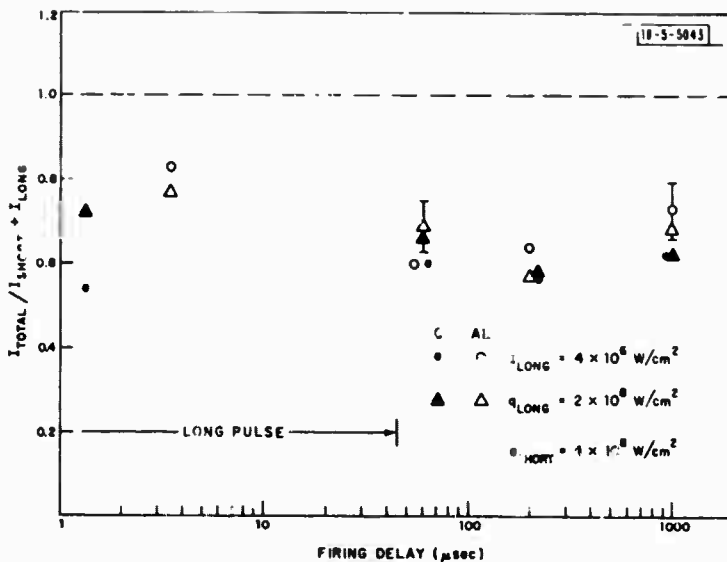


Fig. I-35. Total impulse delivered to 0.38-cm-diameter carbon and aluminum targets for double-pulse firing normalized by the impulse delivered by each pulse when fired separately. These data were taken with the long pulse as the precursor. The error bars denote the estimated maximum error and each plotted point is an average of from three to five separate measurements.

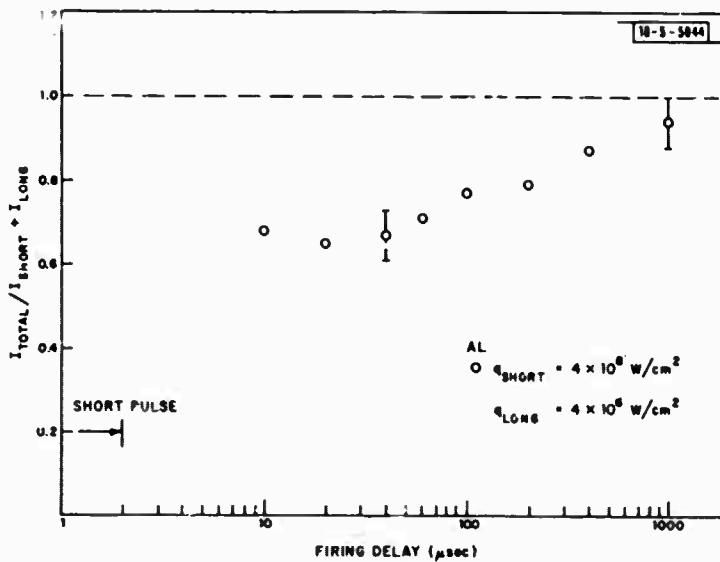


Fig. I-36. Normalized impulse delivered to 0.38-cm-diameter aluminum target with the short pulse as the precursor. The error bars denote the estimated maximum error and each plotted point represents an average of three to five separate measurements.

total impulse is seen to be just beginning to recover after a decay of 1 msec. Results for the case in which the short pulse was the precursor are shown in Fig. 1-36. Here, the impulse delivered to the aluminum target shows a steady increase and takes on the order of a msec to "recover."

Previous double-pulse impulse measurements on small lead targets presented by Hall<sup>30</sup> indicated about a 50-percent enhancement of the impulse delivered by the second pulse after about a 50- $\mu$ sec delay. Hall's double-pulse laser system was such that each pulse had an energy of about 15 J, pulse lengths of about 25  $\mu$ sec, and power densities of a few times  $10^7$  W/cm<sup>2</sup> incident on the target. We did not find any significant enhancement with either aluminum or carbon targets although it should be noted that our experiments were performed with power densities which were an order of magnitude greater and less than those used by Hall.

We conclude from these results that the plasma resulting from the precursor pulse tends to cause the energy in the second pulse to be absorbed in a large volume thereby leading to a greatly reduced peak pressure at the target and also decreasing the total momentum transferred to the target. This view is supported by the fact that, in addition to the reduced peak pressure, the pressure pulse due to the second laser pulse was both delayed and broadened in the double-pulse mode. The delay times required for recovery of peak pressure and impulse to those expected for single-pulse cases were found to be on the order of 1 msec for the experimental conditions reported here.

J. E. Lowder  
L. C. Pettingill

## 2. Hydrodynamic Effects in Double-Pulse Measurements

### a. Introduction

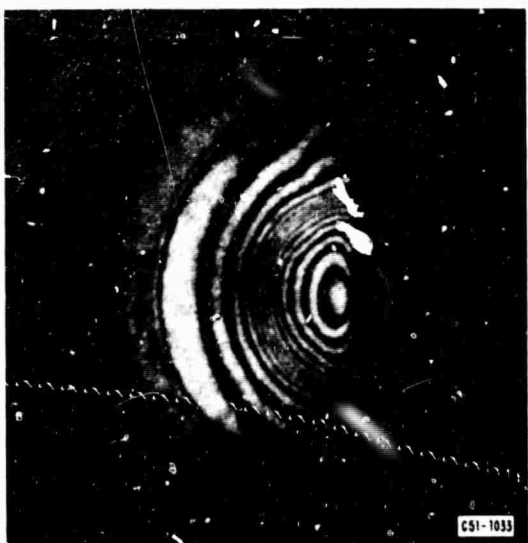
To supplement the pressure and impulse measurements of the response of a target to two 10.6- $\mu$ m laser pulses (see Sec. I-C-1) we have undertaken an examination of the hydrodynamic and plasma environment through which the second pulse must travel. We have further examined the velocity of the luminous front of the second pulse and correlated its motion with the effects of this environment. We have found that both the lowered neutral density and increased electron density in the region of the target lead to a rapid motion of the luminous front away from the target (LSD wave and breakdown wave). This rapid motion can account for the impulse and pressure decoupling noted earlier.

### b. Interferometry

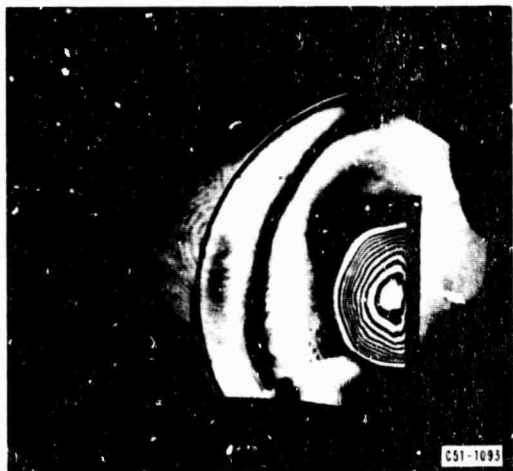
The interferometer used in this experiment is the same Mach-Zehnder interferometer described in the Optics Research Report<sup>3</sup> with only the 5145- $\text{\AA}$  argon laser used as a light source. What is measured then is the contribution to the index shift both from electrons and heavy ions and neutrals.

Two types of laser pulses were examined. The first pulse in a double-pulse experiment was typically about 40  $\mu$ sec long, at an intensity of 1 to  $5 \times 10^6$  W/cm<sup>2</sup>. The second pulse, fired some time delay later, was about 1  $\mu$ sec long with intensities that could be varied up to  $10^9$  W/cm<sup>2</sup>, although for the interferometric investigation intensities of  $5 \times 10^7$  to  $2 \times 10^8$  W/cm<sup>2</sup> were more typical.

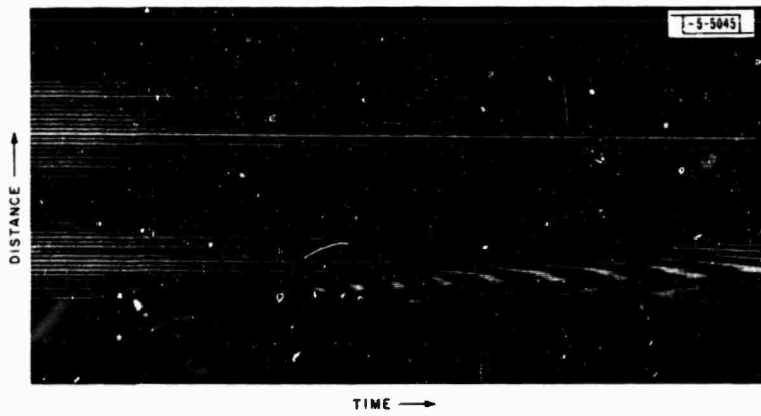
Looking at the long-pulse data first, a volume heating of the plasma occurred (see Sec. I-C-2d) generating a spherical blast wave. Figure 1-37(a-b) shows interferograms of the blast wave at



(a) Two-dimensional interferogram  
for  $\bar{I} = 1.3 \text{ MW/cm}^2$ ,  $\Delta t = 27 \mu\text{sec}$ .



(b) Two-dimensional interferogram  
for  $\bar{I} = 4.8 \text{ MW/cm}^2$ ,  $\Delta t = 60 \mu\text{sec}$ .



(c) Streak interferogram for  $\bar{I} = 1.1 \text{ MW/cm}^2$ .

Fig. I-37. Interferograms of laser-target interaction for long-pulse conditions.

two different intensities and times. Figure I-37(c) is a streak interferogram for the conditions of Fig. I-37(a), showing the index growth normal to the target as a function of time.

Looking at the short pulse alone now, Figs. I-38(a-c) are interferograms at different times showing the evolution of an initial LSD wave [Fig. I-38(a)] into a cylindrical blast wave [Fig. I-38(b)] and finally a spherical blast wave [Fig. I-38(c)]. Note that at late times the shock detaches from the hot core at the target.

Finally, Fig. I-39 shows an interferogram of both pulses, with a time delay of  $\sim 100 \mu\text{sec}$  between the start of pulse 1 and pulse 2, where the interferogram was taken  $110 \mu\text{sec}$  after the start of pulse 1.

An Abel inversion program has been written to reduce the interferometric data (see Sec. I-C-4), and the data reduction is presently under way. Figure I-40 indicates a typical density profile for the long-pulse data taken  $5 \mu\text{sec}$  after the beginning of the long pulse. Notice the density at the target is negative out to about 3.5 mm. This represents the electron contribution. One may write the combined contribution of the free electrons and neutral density to the index of refraction as:

$$F = 1.18 \times 10^{-22} \frac{n_e l_e}{\lambda} + 2.77 \times 10^{-4} \frac{\rho_0 l_n}{\lambda} .$$

Here,  $F$  = fringe shift in wavelengths,  $n_e$  = electron density,  $l_e$  = path length of electrons,  $\rho_0$  = ambient density,  $l_n$  = path length of neutrals, and  $\lambda$  = interferometer wavelength. Using this equation and assigning the entire negative-density contribution to the electrons, we arrive at an electron-density profile and neutral-density profile as shown in Figs. I-41(a) and I-41(b), respectively. There appears to be a relatively uniform sphere of electrons, with  $n_e \sim 4 \times 10^{17} \text{ cm}^3$ . This is consistent with the two-wavelength interferometric measurements previously reported in Ref. 3.

### c. Probe Data

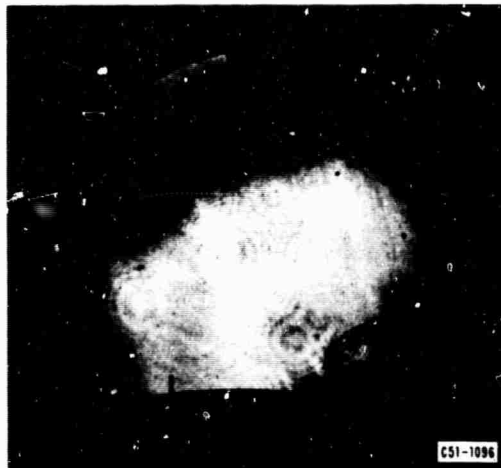
To examine the spatial and temporal history of the electron distribution in front of an aluminum target, a cross-beam,  $10.6\text{-}\mu\text{m}$  probe laser was used (as shown in Fig. I-42). The temporally stable, one-watt CW laser beam was focused to 0.1-mm diameter in the center of the plasma column which is typically several millimeters in diameter. The time-resolved transmission was measured 1, 3, 5, 7.5, 10 and 15 mm in front of the target surface. Figure I-43 shows the spatial dependence of the transmission at the end of the laser pulse and  $20 \mu\text{sec}$  after the end of the pulse. Figure I-44 illustrates the temporal recovery of the transmission 3 mm in front of the target.

If one makes the assumption that for  $10\text{-}\mu\text{m}$  radiation the absorption is due to inverse bremsstrahlung, the absorption coefficient can be used to determine the electron density

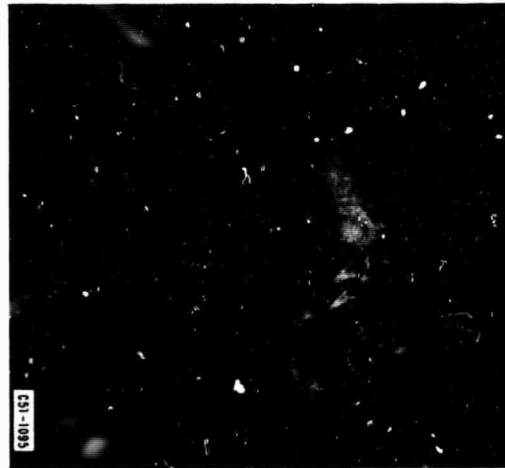
$$\alpha(\text{cm}^{-1}) = 1.6 \times 10^{-37} \lambda^2 n_e^2 T_e^{-3/2} \left( \frac{1}{1 - e^{-h\nu/kT_e}} \right) \frac{kT_e}{h\nu} .$$

Here,  $\alpha$  is the absorption coefficient in  $\text{cm}^{-1}$ ,  $\lambda$  is the probe wavelength in  $\mu\text{m}$ ,  $n_e$  is the electron density in  $\text{cm}^{-3}$ ,  $T_e$  is the electron temperature in eV, and  $\nu$  is the laser frequency. For  $10.6 \mu\text{m}$  and  $T_e \approx 1 \text{ eV}$ ,

$$n_e \approx 2.5 \times 10^{17} \sqrt{\dots} .$$



(a) LSD initiation,  $\bar{I} = 6 \times 10^8 \text{ W/cm}^2$ ,  
 $\Delta t = 1 \mu\text{sec}$ .



(b) Cylindrical blast wave stage,  
 $\bar{I} = 2.8 \times 10^8 \text{ W/cm}^2$ ,  $\Delta t = 40 \mu\text{sec}$ .



(c) Spherical blast wave stage,  $\bar{I} = 2.2 \times 10^8 \text{ W/cm}^2$ ,  $\Delta t = 100 \mu\text{sec}$ .

Fig. I-38. Two-dimensional interferograms of laser-target interaction  
for short-pulse conditions.

Fig. I-39. Two-dimensional interferogram of double-pulse laser-target interaction.

Pulse 1:  $\bar{I} = 1.3 \text{ MW/cm}^2$ ;  
 $\tau_p = 40 \mu\text{sec}$ .  
Pulse 2:  $\bar{I} = 1.1 \times 10^8 \text{ W/cm}^2$ ;  
 $\tau_p = 1 \mu\text{sec}$ ,  
 $\Delta t = 100 \mu\text{sec}$ .

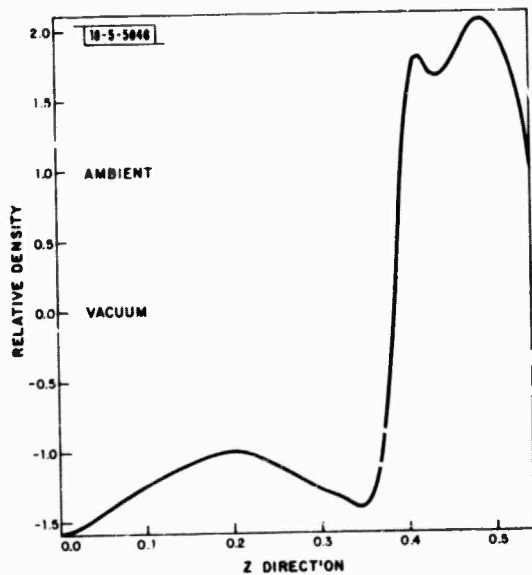


Fig. I-40. Plot of  $n - 1/n_0 - 1$  vs radial distance obtained by Abel inversion of a spherically symmetric distribution similar to Fig. I-38(a).  $\bar{I} = 2 \text{ MW/cm}^2$ ,  $\Delta t = 5 \mu\text{sec}$ .

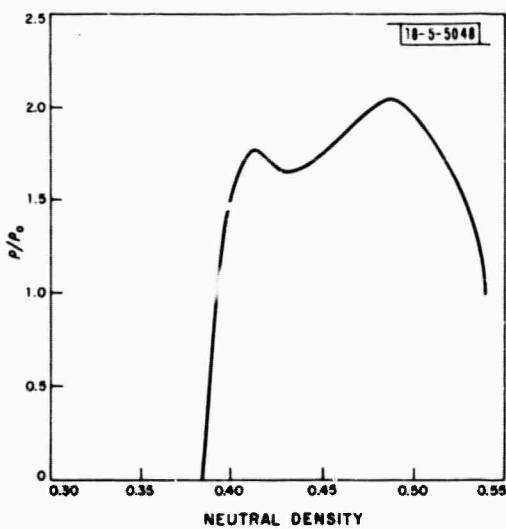
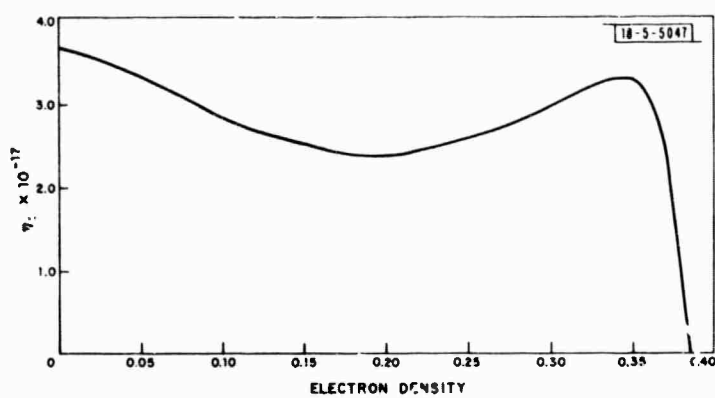


Fig. I-41. (a) Plot of  $n_e$  vs  $r$  from data in Fig. I-38(a). (b) Plot of  $\rho/\rho_0$  vs  $r$  for data in Fig. I-38(a).

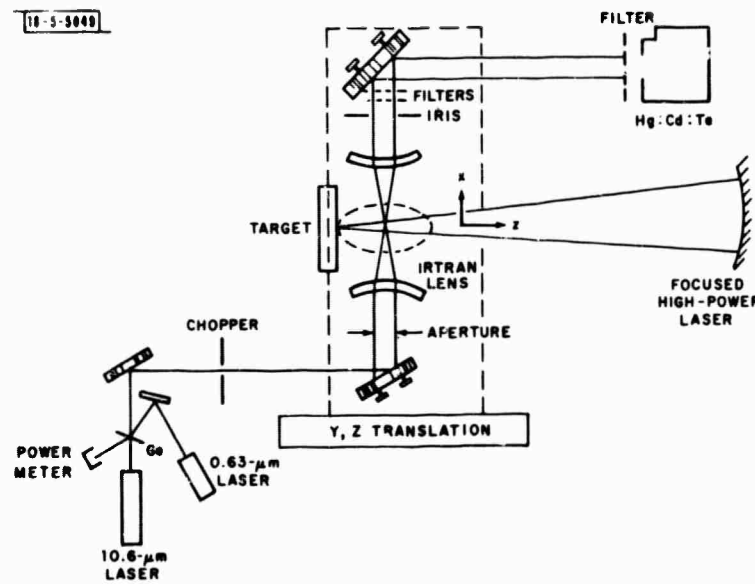
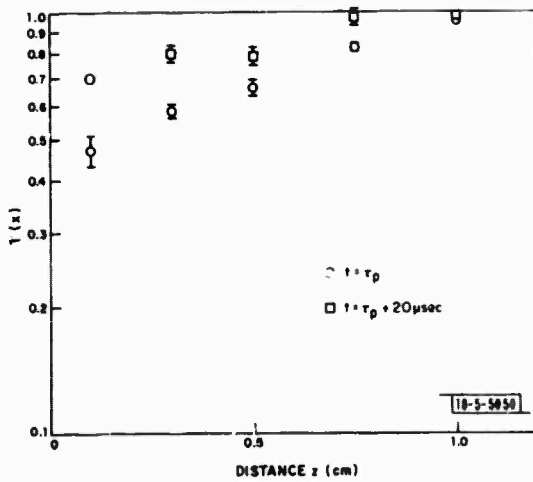


Fig. I-42. Schematic of 10.6- $\mu\text{m}$  cross-beam transmission experiment.

Fig. I-43. Transmission through the laser-generated plasma column plotted as a function of  $z$ , the distance from the target, for  $\Delta t = \tau_p$  the pulse length and  $\Delta t = \tau_p + 20 \mu\text{sec}$ ,  $\tau_p \sim 45 \mu\text{sec}$ ,  $I \sim 2 \text{ MW/cm}^2$ .



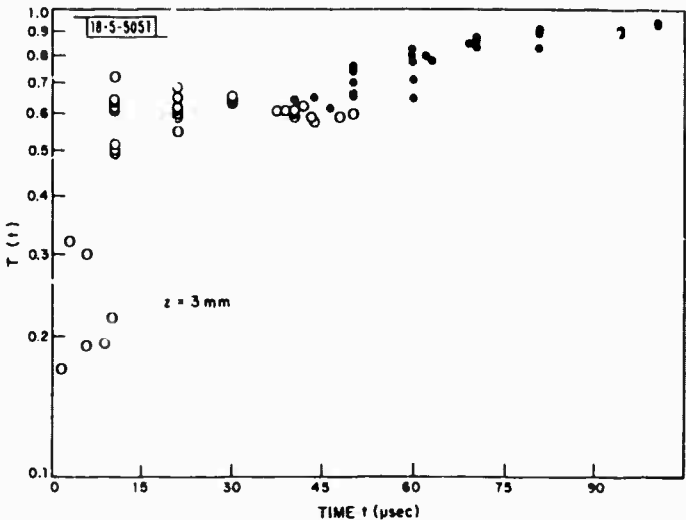


Fig. I-44. Plot of transmission through plasma column as a function of time for  $z = 3$  mm. The filled symbols indicate the laser is still on. The open symbols are appropriate to the laser's being off.

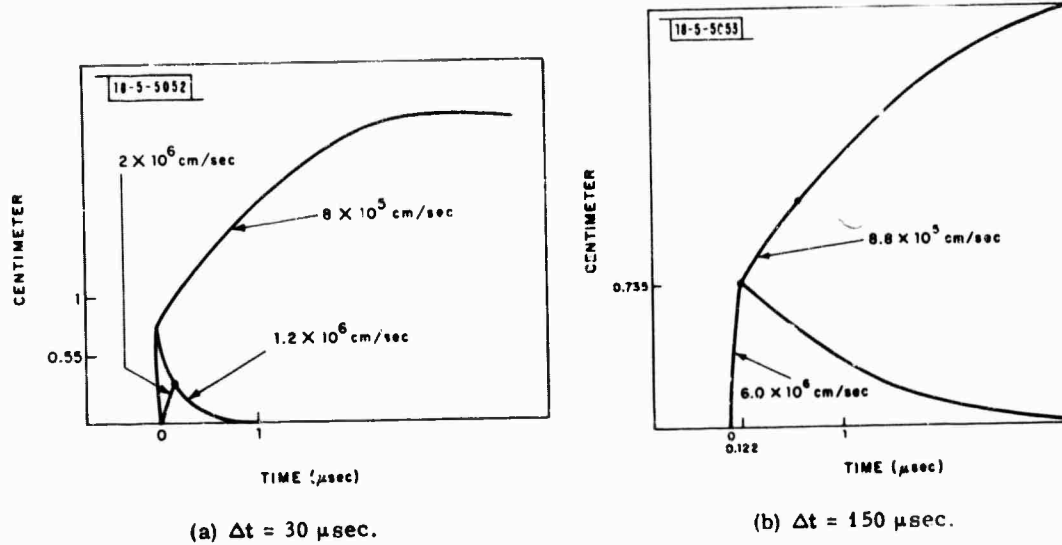
From the transmission curves of Figs. I-43 and I-44, we can derive values of  $\alpha t$ . Assuming a uniform sphere of electrons with radius of about 1 cm (i.e., where the absorption is  $\sim 0$  in Fig. I-43), we find electron densities of  $2$  to  $3 \times 10^{17}/\text{cm}^3$  at the target for times from 40 to 60  $\mu\text{sec}$  after the start of the pulse. The numbers are consistent with the values found interferometrically.

#### d. Streak Data

A series of experiments was run to determine the effects of the neutral and electron density left by the first pulse on the dynamics of the second pulse. For these experiments the first pulse was 40  $\mu\text{sec}$  long, and the luminous velocity of a second pulse was examined as a function of time delay between the two pulses and intensity of the second pulse.

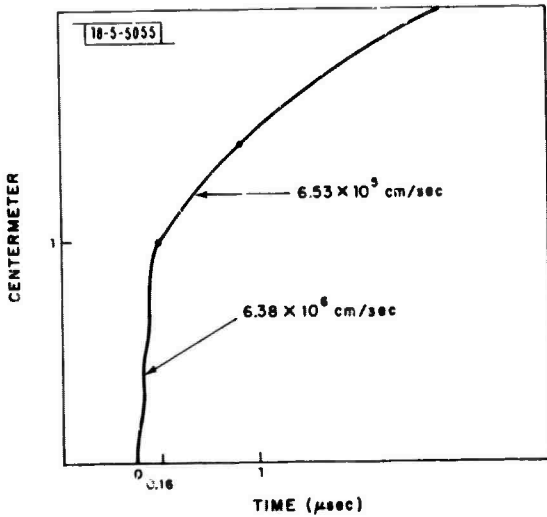
Figure I-45 shows a sequence of streak photographs at time delays of 30 to 400  $\mu\text{sec}$  between the start of pulse 2 and the start of pulse 1. For the early time history, while the first laser pulse is still on, breakdown apparently initiates at the edge of the plasma produced by the first pulse, and a normal LSD wave is launched at this point. In addition, enough energy is transmitted through the volume absorbing plasma to launch a weak LSD wave from the target surface. For times from  $\sim 100$  to 400  $\mu\text{sec}$ , a very rapid wave is launched from the target ( $v \sim 6 \times 10^6 \text{ cm/sec}$ ). There exist two possible causes for this high velocity. First, it might be an LSD wave launched in the low-density air left behind the first pulse. However, since the velocity is about five times faster than might be expected in ambient air, this would indicate a residual density of  $\sim 0.008$  amagat ( $v \sim 1/\rho^{1/3}$ ). It is hard to measure the density to this accuracy at the target because of the electron contribution to the index change.

The electrons themselves may be a contributor to the velocity of the luminous front since, as Smith<sup>31</sup> has shown, the threshold for breakdown decreases with electron density. For the high-intensity second pulse ( $\sim 10^9 \text{ W/cm}^2$ ), a breakdown wave can be launched back towards the laser. This wave will continue until the intensity drops to the point where it is below the breakdown threshold for that distance from the focal point. At this point a normal LSD wave will be formed.

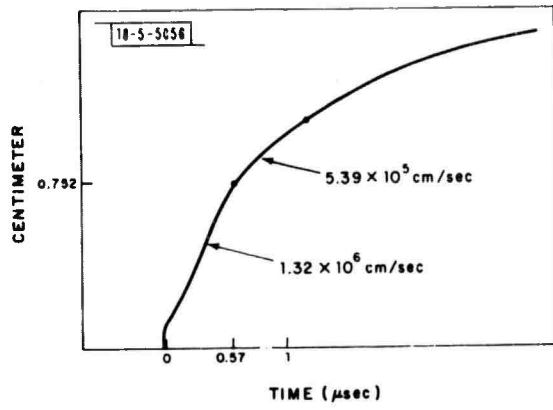


(c)  $\Delta t = 400 \mu\text{sec}$ .

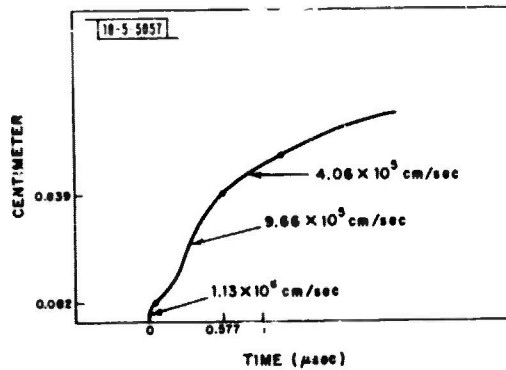
Fig. 1-45. Sketches of streak photographs of luminous plasma fronts resulting from double-pulsed laser-target interactions.  $I_1 \sim 2 \text{ MW/cm}^2$ ,  $I_2 \sim 8 \times 10^8 \text{ W/cm}^2$ . Exposure during pulse 2  $\Delta t$  after pulse 1.



$$(a) I_2 = 7.2 \times 10^7 \text{ W/cm}^2$$



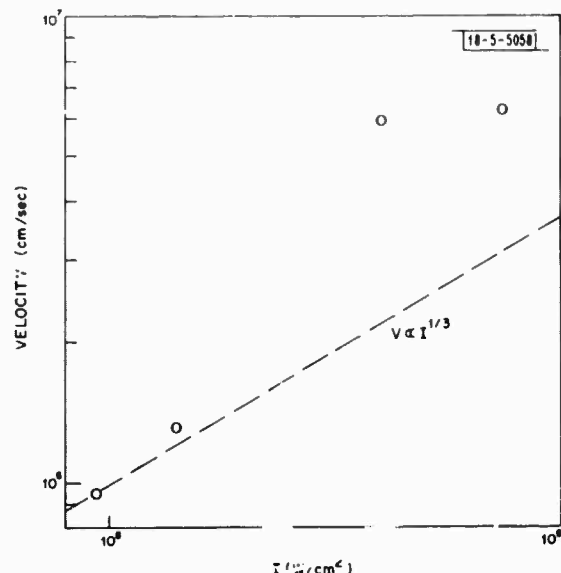
$$(b) I_2 = 1.9 \times 10^8 \text{ W/cm}^2$$



$$(c) I_3 = 7.2 \times 10^8 \text{ W/cm}^2$$

Fig. I-46. Sketches of streak photographs of luminous plasma fronts resulting from double-pulsed laser-target interaction. Exposure during second pulse that occurs 85  $\mu$ sec after first pulse.  $I_1 \sim 2 \text{ MW/cm}^2$ .

Fig. I-47. Plot of luminous front velocity as a function of  $I$  for  $\Delta_t = 85 \mu\text{sec}$ .



Some evidence as to which mechanism is more appropriate can be obtained from Fig. I-46, in which streak data are shown which were taken at a fixed time ( $85 \mu\text{sec}$ ) after the start of pulse 1 for a number of different intensities. Using these streak data, we have plotted the initial velocities as a function of intensity at the target (Fig. I-47). Since we expect the hydrodynamics to be the same for all three intensities, the velocities should vary as  $I^{1/3}$  if an LSD wave were launched in all cases. Notice for lower intensities the  $I^{1/3}$  behavior becomes more appropriate. However, for intensities above  $3 \times 10^8 \text{ W/cm}^2$ , the dependence on intensity is much stronger which is characteristic of a breakdown phenomena.

The LSD velocities in the lower intensity streak photographs indicate a residual density of 0.2 to 0.5 amagat  $85 \mu\text{sec}$  after the firing of pulse 1. Thus, all we really know about the residual neutral density at the target at  $5 \mu\text{sec}$  is that the density is 0.2 amagat or less. However, the difference between assuming vacuum at the target and assuming 0.2 amagat is less than a factor of two in the electron density.

#### e. Conclusions

We have examined the physics involved when two laser pulses interact with a target. In particular, we have examined the target environment left by the first pulse. What is left at a time of the order of 10 to 100  $\mu\text{sec}$  after the first pulse is a low-density ( $\lesssim 0.2$  amagat) electron-rich ( $n_e \approx 10^{17}/\text{cm}^3$ ) environment. For second pulses with intensities of  $\sim 10^8 \text{ W/cm}^2$  an LSD wave is launched with a velocity characteristic of the low-density environment. For intensities of  $10^9 \text{ W/cm}^2$ , a breakdown wave is launched in the electron-rich environment at the low breakdown threshold characteristic of such a medium. This wave travels with a high velocity which, in general, will be a function of geometry of the experiment. In either case, there is a strong decoupling of the radiation from the target consistent with the pressure-impulse results reported elsewhere.

H. Kleiman  
R. W. O'Neil  
L. C. Pettingill

### 3. Empirical Modeling of Vapor Sphere Expansion from Laser-Exploded Water Droplets

When water spheres are irradiated with a pulsed laser beam, the energy absorption leads to a shock formation traveling radially out from the drop at a velocity faster than the sound velocity

and to a vapor sphere which follows at a velocity (initially less than the speed of sound) which monotonically decreases in time.<sup>32,33</sup> If a precursor laser pulse is used to clear a fog, a subsequent pulse would experience beam distortion primarily due to the medium index fluctuations induced by these vapor spheres. We have used the data assembled by Kafalas *et al.*<sup>31,32</sup> to parameterize empirically the vapor sphere expansion.

We tested as possible dependence of the vapor sphere velocity with time, functions that yield exponential decays and decays inverse to some power of time [i.e.,  $v(t) = v_0 e^{-t/\Delta t}$  or  $v(t) = v_0(t + t_0)^{-m} \cdot t_0^m$ , where  $v_0$ ,  $\Delta t$ ,  $t_0$ , and  $m$  are parameters to be determined]. We then fitted the parameters to the measured values of vapor sphere size as a function of time by integrating the velocity function with respect to time. We found that the exponential velocity decay was much too fast, and the best fit for the inverse time decay yields an optimum fit for a radius expansion of the vapor sphere:

$$a(t)_{\text{vapor sphere}} = 0.26 \text{ mm ln}(\frac{1.079 + t}{1.079}) + r_w$$

where  $t$  is in  $\mu\text{sec}$  and  $r_w$  is the initial water vapor size. The rate of expansion as measured from the experimental data displays no dependence on initial droplet size. The matching has been done for a range of initial particle radii and for times out to about 40  $\mu\text{sec}$  after laser pulse incidence.

These data correspond to a laser pulse of 10 MW/cm<sup>2</sup> and to a half-width of ~300 nsec. There is some indication that the time dependence scales inversely with power, i.e., as the power is increased, the rate of expansion correspondingly increases, but we do not have sufficient data to make a quantitative determination. We hope soon to explain the observed expansion rates on a theoretical basis.

H. Granek

#### 4. Abel Inversion Program

In support of the interferometric data described in Sec. I-C-2, we have developed an Abel Inversion Code to reduce the phase shifts to density contours. For a cylindrically symmetric density variation in a material of uniform composition, the change in the density at a point  $y$  away from the axis of symmetry is given by Abel's inversion formula

$$\Delta\rho = \frac{-\lambda\rho_0}{(n_0 - 1)\pi} \int_y^{r_n} \frac{\frac{\partial\delta}{\partial r} dr}{(r^2 - y^2)^{1/2}}$$

where  $\delta$  is the phase shift.

Here it is assumed the change in the density is related to the change in the index of refraction by

$$\frac{\Delta n}{n_0 - 1} = \frac{\Delta\rho}{\rho_0}$$

where  $n_0$  and  $\rho_0$  are the ambient index and density, respectively. The data from interferograms (cf. Sec. I-C-2) are smoothed by a cubic spline interpolation and the numerical derivative is subsequently expanded in a basis set of linear splines defined by

$$w_i(r) = \frac{r - r_{i-1}}{r_i - r_{i-1}} \quad \text{for } r_{i-1} \leq r \leq r_i$$

$$w_{i-1}(r) = \frac{r_i - r}{r_i - r_{i-1}} \quad \text{for } r_{i-1} \leq r \leq r_i$$

The resulting expansion for  $\delta'$  is given by

$$\delta'(r) = \sum_i w_i(r) \delta_i' .$$

Substituting into the inversion formula and evaluating the remaining derivatives results in the following expression for the density change at  $y_j$

$$\Delta\rho(y_j) = \frac{-\lambda\rho_0}{(n_0 - 1)\pi} \left\{ \sum_{i=j+1}^N \frac{\delta_{i-1}' r_i - \delta_i' r_{i-1}}{(r_i - r_{i-1})} \ln \left[ \frac{r_i + \sqrt{r_i^2 - y_j^2}}{r_{i-1} + \sqrt{r_{i-1}^2 - y_j^2}} \right] \right. \\ \left. + \sum_{i=j+1}^N \frac{\delta_i' - \delta_{i-1}'}{r_i - r_{i-1}} [ (r_i^2 - y_j^2)^{1/2} - (r_{i-1}^2 - y_j^2)^{1/2} ] \right\} .$$

This inversion procedure has been tested with Gaussian phase shift variations for which the inversion integral has a closed form. The results indicate that this code will invert phase shifts with an error limited by the number of points in the linear spline expansion of  $\delta'$ . For an expansion containing 90 points the error is less than 0.5 percent - well below that needed for this analysis.

Since the smoothed data are similar to a sum of Gaussian curves, it is assumed the resulting inversions reflect accurately the density variations for such data. The largest source of numerical error in the whole procedure is in initially smoothing the raw data.

D. L. Mooney

#### D. DEVICES

##### 1. Dual 500-J Electron-Beam Laser

The dual 500-J e-beam laser is in the final stages of checkout. The system has been completely assembled and is now operational. It is currently utilizing the original Lexan and the interim Lucite sustainer cavities. Aluminum sustainer cavities have been delivered and will be installed early in 1974.

The device is complete except for the automation of certain auxiliary sequencers. A new digital fast sequencer to provide timing between the two laser operations and to facilitate operator control of the firing sequence is ready for test. Provisions for selectively disabling parts of the interlock chain for test purposes will be provided in a modification now being designed.

Each laser has been tested independently and has operated successfully with good beam quality. Double-pulse operation has been achieved.

The Lincoln Laboratory two-pulse laser facility has been constructed to study the propagation and target interaction phenomena of multiple-pulse lasers for an arbitrary interpulse separation. For common-path problems such as air breakdown, thermal blooming in a stationary air column, precursing, fog hole boring, and subsequent propagation, two 250-J beams are obtained via a germanium beam splitter (half the energy is lost by using the beam splitter). For applications where a small angular offset is tolerable (target interaction) or desirable

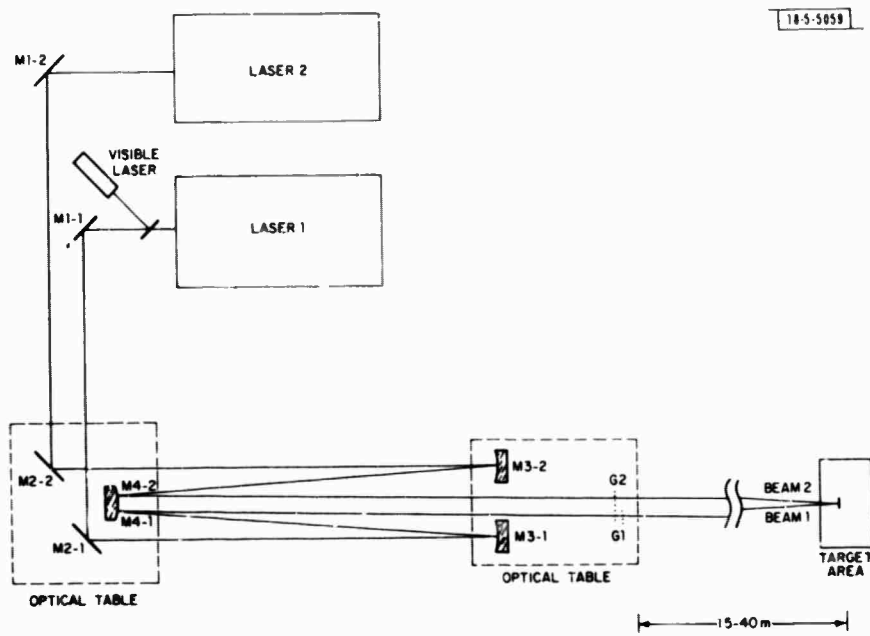


Fig. I-48. Optical schematic of two-pulse laser facility.

TABLE I-2 PHYSICAL PARAMETERS USED IN CALCULATIONS IN THIS PAPER	
HF Pressure	$\sim 0.1$ torr ( $3.4 \times 10^{16}$ molecules/cc)
H <sub>2</sub> Pressure	$\sim 200$ torrs ( $6.8 \times 10^{18}$ molecules/cc)
Argon Pressure	$\sim 200$ torrs
Electron Number Density	$5 \times 10^5$ /cc
Ionizing Pulse	< 5 $\mu$ sec

(blooming interaction between two slewed pulses), two 500-J pulses are available as indicated in Fig. I-48. In this configuration, beam diagnostics are obtained using two high-transmittance gratings angularly displaced to provide a complete independent analysis on each beam. In the common-path arrangement, time-resolved measurements on each pulse are required. The optical range has 45 m of straight path or 90 m from a single reflection. A 30-m-long, 50-cm-diameter evacuable range is available for controlled atmospheric propagation or vacuum target interaction experiments.

A. J. Morency  
R. W. O'Neil

## 2. Other Lasers

### a. H<sub>2</sub>-HF Electron-Beam Laser System

The objective of this project is to obtain a long-pulse (1- to 5- $\mu$ sec) HF laser with 1 to 10 joules output energy. The approach will be to excite electrically a gas mixture containing H<sub>2</sub> and HF and, therefore, to utilize electron pumping of H<sub>2</sub> with a subsequent resonant transfer to HF as the basic inverting process of the HF laser. The electrical excitation will be done with a cold-cathode electron-beam-stabilized discharge system of commercial manufacture.

The basic physical principles of the laser were described in the last QTS<sup>3</sup> and in Ref. 34. Here we will describe only the most recent progress on the project and, in particular, work on understanding the laser using both a theoretical and experimental approach. Also, brief mention will be made of the preparatory work for the arrival of the large e-beam system.

#### (1) Modeling of an H<sub>2</sub>-HF Discharge

The simplest and most direct way to excite preferentially the H<sub>2</sub> vibrational levels is to use an electric discharge with a suitably tuned ratio of electric field to number density (E/N). For the case of the H<sub>2</sub>-HF mixture, tunability of E/N is best obtained with an e-beam preionized sustainer voltage. Because the cross section for vibrational excitation of H<sub>2</sub> by electrons is comparatively small (e.g., a factor of 8 less than CO), it is necessary to have a large electron density in the sustained discharge. Inspection of commercially available electron-beam guns shows that a cold-cathode gun gives the highest integrated current density for the 1- to 5- $\mu$ sec pulse lengths which are of interest to Lincoln Laboratory.

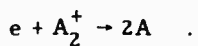
Because of the anticipated high rate of attachment in HF gas, it is desirable to use an H<sub>2</sub>-HF mixture which contains as little HF as possible from the viewpoint of a workable small-signal gain. Prior work on kinetics also shows that such a low HF concentration is also desirable if one is to have a slow rate of vibrational-to-translational energy transfer between two HF molecules. However, use of such a low-Z (atomic number) mixture is not desirable if one wishes to achieve a high ratio of electron density to hydrogen density, a ratio which is necessary for rapid electron pumping of the H<sub>2</sub> vibrational levels.

This situation may be rectified in our case by addition of argon (Z = 19) to the mixture. Not only will argon add the necessary stopping power to the mixture, but it also will leave the rates of the various modes of vibrational relaxation essentially unaltered. This results from the fact that an inert atomic gas can relax vibrational levels only by the highly nonresonant process of vibrational-to-translational energy transfer. In addition, as will be discussed in the following section, argon will reduce the temperature rise in the H<sub>2</sub> gas.

In order to estimate the electron density in the typical gas mixture shown in Table I-2, it is first necessary to estimate the relative rates of the various channels of electron loss. Diffusion

may be immediately eliminated because of the high total gas pressure. Because of their low electronegativity the attachment rates of argon and H<sub>2</sub> are vanishingly small. The attachment of HF is not known; however, the attachment rates in HCl and HBr have been measured by Buchel'nikova.<sup>35</sup> If we conservatively estimate its rate to be the same as HCl and we use the HF gas pressure of Table I-2, we find an attachment rate of  $1.4 \times 10^6 \text{ sec}^{-1}$ .

The recombination rate of the mixture will result primarily from the process



Its characteristic rate will be  $(7 \times 10^{-7}) (n_e)$ . If we assume  $n_e \approx 5 \times 10^{13}$  (to be verified below) we find the characteristic rate to be  $3 \times 10^7 \text{ sec}^{-1}$ . It is apparent, therefore, that recombination is the primary means of electron loss for the discharge under consideration.

A consistency check of the above discussion can now be made by verifying that an  $n_e \approx 5 \times 10^{13}$  is a reasonable electron density to attain with the electron-beam and discharge parameters envisaged here. Since the recombination time is fast compared to the inverse of a typical pulse duration time, we may assume a steady-state electron density exists; then,  $n_e \approx \sqrt{S/\alpha}$  where S is the electron production rate and  $\alpha$  is the recombination coefficient. Using the tabulated stopping power of argon, we can calculate  $S \approx 10^{21}$  electrons/second. For argon molecular recombination,  $\alpha = 7 \times 10^{-7}$ , and thus  $n_e \approx 5 \times 10^{13} \text{ cm}^{-3}$  is reasonable.

As shown in Ref. 34, the HF gain is sensitive to both the vibrational and translational rotational temperature of the gas mixture. Further, the rate and fractional power transfer to each of these modes depends nonlinearly on the E/N of the discharge. As a result, it is not possible to calculate the magnitude or temporal behavior of gain without a complete solution of the time-varying problem. Here we describe the results of a computer modeling of the discharge which, while not yet complete, is sufficiently developed to allow pinpointing of the specific problems in the laser design as well as their possible solutions.

The basic element of our computation is calculation of the electron energy distribution in the discharge. The overlap of this distribution with the cross sections of each of the processes of interest will determine the rate of that process. To determine the distribution we have solved the Boltzmann equation much in the manner of Frost and Phelps<sup>36</sup> (and later Nighan<sup>37</sup>). The vibrational cross sections used in this calculation are those of Schultz;<sup>38</sup> all other cross sections are from Frost and Phelps. Except where noted, the physical parameters used in the calculation are those given earlier in Table I-2.

Figure I-49 shows the initial rate of electron pumping of the H<sub>2</sub> vibrational levels, i.e., the pumping rate assuming no excited H<sub>2</sub> molecules, for various values of E/N. From this figure it is apparent that if one wishes to pump on the scale of 10  $\mu\text{sec}$  or less, then an E/N of less than  $10^{-16} \text{ V/cm}^2$  is unacceptable.

However, in order to obtain an accurate representation of the pumping rate, it is essential to take into account the change in the electron distribution with the degree of excitation in the gas. This arises because of the fact that as the population in the first vibrational level rises, superelastic collisions can then give energy back to the electrons.

Thus, to determine how the vibrational population changes in time, we must solve a nonlinear rate equation such as

$$\frac{dH_2(v=1)}{dT} = H_2(v=0) n_e \int f(u, N_0, N_1) \sigma(u) u du - H_2(v=1) n_e \int f(u, N_0, N_1) \sigma'(u) u du \quad (I-6)$$

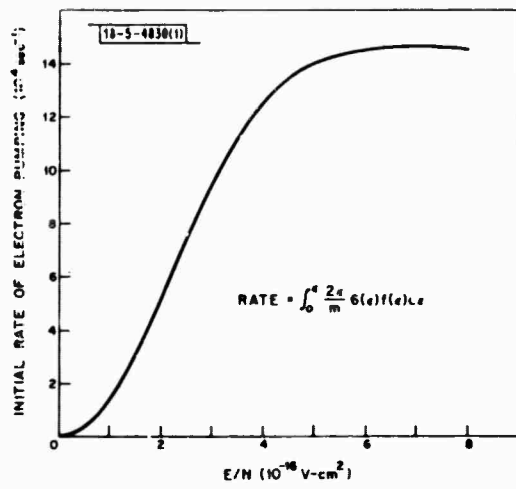


Fig. I-49. Rate of electron pumping of the  $H_2$  vibrational levels assuming an  $H_2$  vibrational temperature of  $300^\circ K$  as a function of electric field to neutral particle density.

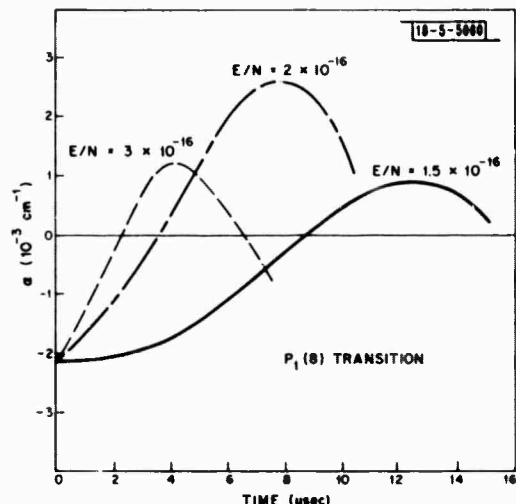


Fig. I-50. Calculated time-dependent gain of the  $P_1(8)$  transition assuming 0.1 torr of HF and 200 torrs of  $H_2$  as a function of electric field to neutral particle density.

where  $N_{0,1}$  is population in the zeroth and first vibrational levels, respectively;  $u$  is the electron energy in  $eV$ ;  $(u, N_0, N_1)$ ,  $(u)^{1/2}$  is the electron energy distribution (a function of  $u$  and vibrational level population); and  $\sigma(u)$  and  $\sigma'(u)$  are the cross sections for electron excitation and de-excitation of the  $H_2$  vibrational levels, respectively. If the degree of vibrational excitation is small, we may neglect all excited levels higher than the first, and (I-6) is the only rate equation to be solved.

Notice that since the vibrational equilibration time for  $H_2$  and HF is rapid (300 nsec) compared to the anticipated pumping pulse length, we can determine the population of HF in the first vibrational level by assuming intermolecular vibrational equilibrium exists. The results of a calculation of HF gain on the  $P(8) v = 1 \rightarrow v = 0$  transition as a function of time for three values of  $E/N$  are shown in Fig. I-50. It is apparent, first of all, that the rate of excitation is an extremely sensitive function of  $E/N$ . Therefore, it is vital to have the freedom to tune the discharge  $E/N$  as would exist in an e-beam sustained discharge. Second, the limitation on low values of  $E/N$  is not simply pumping time. Rather, the fraction of discharge energy which goes into gas heating (i.e., translational and rotational energy) increases as one goes toward lower values of  $E/N$ . As a result, the tendency is for a higher gas temperature (and hence lower gain) for a given vibrational temperature as one decreases  $E/N$ . This is illustrated in Fig. I-50 by the smaller gain obtained in the curve for  $E/N = 1.5 \times 10^{-6} V/cm^2$  than that for  $2 \times 10^{-6} V/cm^2$ . A third observation is that if one goes toward higher  $E/N$ , discharge energy is then wasted on the next higher inelastic process (HF and  $H_2$  dissociation).

The problem of gas heating is, in reality, a more serious problem than shown in Fig. I-50. Our model shows that in a pure  $H_2$ -HF mixture all P-branch transitions with  $J < 8$  do not exhibit gain primarily because of the effects of gas heating. Hence, control of gas heating is considered a major experimental difficulty in design of this laser. If, however, one allows for the presence of argon in the gas mixture, the problem of gas heating is seen to be much less severe. Since the first inelastic cross section in argon occurs at 11 eV and since the average electron energy

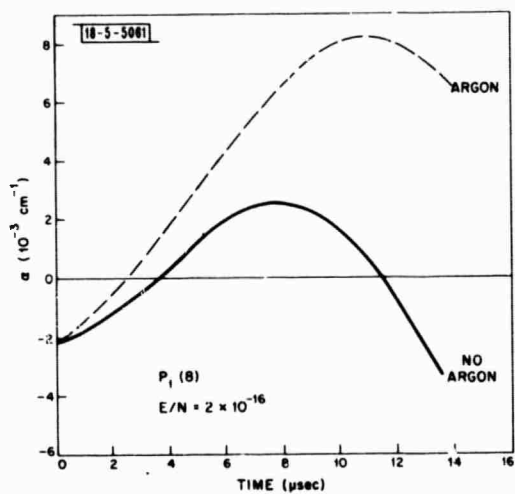


Fig. I-51. Effect on the time-dependent gain of addition of 200 torrs of argon to the mixture of Fig. I-50.

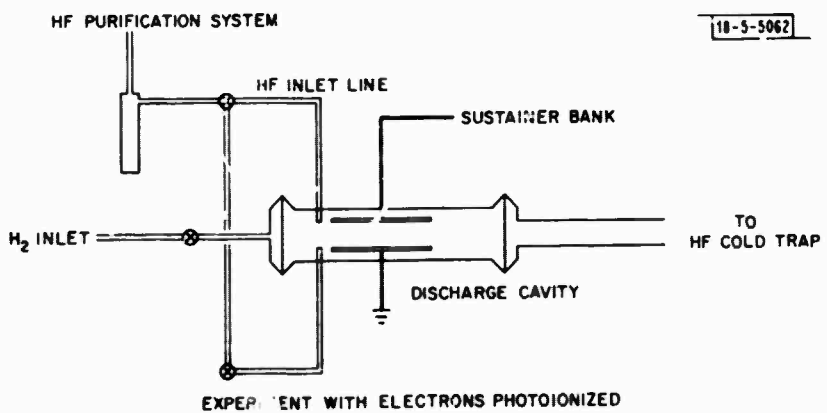


Fig. I-52. Apparatus used for scaled-down modeling of H<sub>2</sub>-HF laser system.

for a typical  $H_2$ -HF plasma considered above is 1 eV, argon can effect such a discharge only via its elastic cross section (or cross section for momentum transfer). However, in the region of 1 eV or less, the Ramsauer minimum in the argon elastic cross section makes it much smaller than the corresponding cross section in  $H_2$ . As a result, for a gas mixture of equal parts of  $H_2$  and A for an E/N ratio giving an average energy of 1 eV or less, the presence of A has no effect on the electron energy distribution. Further, there is no heating of argon by momentum transfer collisions with electrons because  $M_e/M_A \ll M_e/M_{H_2}$  where  $M_e$  is the mass of the electron, etc. Thus, the chief effect of adding argon is to increase the heat capacity of the gas mixture. The dramatic effects of adding argon to the gas mixture are shown in Fig. I-51. We see that by decreasing the rate of temperature rise, the addition of argon causes the gain to rise faster and to attain a greater peak magnitude than without it.

In conclusion, we again stress that this study is by no means complete yet. To be included in our model are a more detailed analysis of the effects of an argon additive, recently published revised cross-section data for  $H_2$  vibrational and rotational levels, and investigation of the effects of considering more than two vibrational levels for both the  $H_2$  and HF vibrational manifold. We summarize the results of this section as follows:

- (a) Within the limitations of our present model, small-signal gains of practical magnitude ( $\sim 0.002/cm$ ) can be obtained in a cold-cathode electron-beam sustained discharge containing  $H_2$ , HF, and argon.
- (b) The most serious difficulty which has become apparent in the study thus far is that of gas heating. However, its effects can be reduced by judicious addition of argon.

R. Osgood  
D. L. Mooney

## (2) Experimental

Although every attempt has been made to include all significant detail in the above numerical calculations, uncertainties as to the particular values of many cross sections make it advisable to check the predictions of the model with a small-scale experimental apparatus. Such an apparatus has been constructed and is shown schematically in Fig. I-52. Note, first, that the system is constructed of components resistant to chemical reaction by HF. Gases are flowed through the system so that any discharge byproducts will not remain in the discharge region after one pulse cycle. A cold trap is used to remove HF from the  $H_2$ -HF mixture prior to its entering the vacuum pump.

Electrical excitation of the gas mixture is accomplished by applying a DC sustainer voltage to the two stainless steel electrode plates within the sample cell and then generating a pulse of electrons within the gas, thus allowing current to flow. Since one of the purposes of this apparatus is to simulate a larger cold-cathode system, the ideal way to generate the electrons within the gas is to utilize a small cold-cathode e-beam. Currently, such a device is being tested. If it works satisfactorily, it will be incorporated in the above apparatus. Meanwhile, preliminary experimentation has been done using photoionization with a tri-n-propylamine seeded mixture. While such a seeded mixture is not ideal from the standpoint of chemical stability, it can provide useful information on rates of attachment and recombination in  $H_2$ -HF mixtures. As mentioned in the previous section, such information is necessary if one wishes to calculate the electron

density in an e-beam preionized plasma. The results of the experiments with the photoionized mixture show that for the typical gas mixtures given in Table 1-2 dissociative recombination with argon molecular ions is the process limiting the electron density. Electron attachment to HF does not appear to be a competitive process.

R. M. Osgood

### (3) Preparation for Large Cold-Cathode System

To prepare for the arrival of the large e-beam system from the subcontractor, a number of pieces of auxiliary apparatus have been designed, fabricated, and tested. Among these are two transverse-discharge HF lasers. These will be used as probes for measurement of gain in the larger high-pressure device. Also fabricated were various components of the gas-handling and vacuum-exhaust apparatus for that device. Much of the experience gained in building the gas flow system for the smaller H<sub>2</sub>-HF system (described above) has been of use in this phase.

R. M. Osgood  
A. J. Morency

#### b. E-Beam-Initiated HF Laser

The Laser Technology program requires high-energy pulsed HF lasers to perform beam-propagation and surface-effects experiments in the 3-μm region of the spectrum. In order to determine the effectiveness of a repetitively pulsed laser within the limitations of our budget, these experiments will be performed with two pulses, from two distinct lasers, of adjustable time separation. One group of experiments requires two pulses of approximately 200 joules and 200-nsec length. We plan to achieve this goal by using high-intensity, high-energy electron beams to initiate HF chemical lasers.

We are currently building the first of these lasers. The plan is to introduce a 500-keV, 60-nsec electron beam of 20 cm<sup>2</sup> cross section and 250 kA peak current at a small angle to the laser axis. The beam, which will be bent and confined by an axial magnetic field, will initiate the reaction by dissociating a fluorine-bearing compound. Initially, the laser mixture will be SF<sub>6</sub> and C<sub>2</sub>H<sub>6</sub> from which, based on work reported at Maxwell Laboratories<sup>39</sup> and Sandia Laboratories,<sup>40</sup> we can expect at least 60 joules. We have ordered the electron-beam accelerator, which will be delivered in March 1974. The laser and associated components are currently being fabricated and will be ready by that time. Unstable resonator geometry, which has been shown to be useful for high-gain, large-volume lasers, has been incorporated into the design. It is expected that the laser will be operational within two months subsequent to delivery of the electron-beam accelerator. To ensure maximum field homogeneity, a computer program has been written to determine the optimum number of windings per individual coil.

S. Marcus            R. C. Archibald  
A. J. Morency       D. L. Mooney  
W. R. Fanning

#### c. HF Electric-Discharge Laser

Work was continued this period on the eventual development of an electric-discharge HF laser of 10 to 20 joules near diffraction-limited output. Due to excessive arcing in the discharge, the maximum output obtained until this period was 0.13 joule from a 0.2-liter device with 100 joules input - less than 10 percent of that expected. Efforts this period were, therefore, concentrated on solving the arcing problem.

It was decided to use smooth metallic electrodes, shaped for maximum field uniformity, and to improve the discharge by (1) minimizing the combined inductance of the laser and current source, and (2) adjusting the laser mixture so that its impedance matches that of the current source, thus minimizing the time required for energy transfer to the gas and reducing the probability of arcing.

The most dramatic improvement in laser performance resulted from replacing H<sub>2</sub> as a hydrogen atom source with C<sub>2</sub>H<sub>6</sub>. With a mixture of typically 65 torrs SF<sub>6</sub> and 10 torrs C<sub>2</sub>H<sub>6</sub> and an electrical input of 100 joules, an output of 2.25 joules was obtained. This efficiency is comparable to the best obtained from nonchain HF lasers.

During the next period, we plan to test a commercially obtained, low-inductance Marx bank with >500 joules storage in an attempt to increase further the output of the laser. We also plan to use an unstable resonator to optimize its beam quality.

S. Marcus

#### d. H<sub>2</sub>-F<sub>2</sub> Laser

It is possible that the mixture of SF<sub>6</sub> and C<sub>2</sub>H<sub>6</sub> will not yield sufficient energy to provide 200-joule laser pulses which are needed for 3-μm surface effects and propagation experiments. In that event, we will be compelled to use the H<sub>2</sub>-F<sub>2</sub> chain reaction, from which more energy is available. With this reaction, laser pulses can be stretched at a cost of output energy to cover the 1- to 5-μsec pulse-length regime by adjustment of gas pressure. Because of this, such a laser can also serve as a backup for the H<sub>2</sub>-HF laser described in Sec. I-D-2a above.

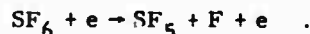
Use of such a corrosive and explosive medium, however, will require stringent construction techniques and safety procedures. In order to develop an expertise for handling H<sub>2</sub>-F<sub>2</sub> mixtures, we plan to build a small flashlamp-initiated H<sub>2</sub>-F<sub>2</sub> laser of roughly 10 joules output capability. To date, we have received almost all of the required components for such a system, and we shall begin assembly in the near future.

S. Marcus  
H. Granek

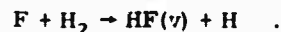
#### e. HF Laser Kinetics

In support of the high-energy HF laser device program, a computer study of the molecular kinetics of the laser has been initiated. The goal is to be able to predict the laser output as a function of the relevant parameters. The following assumptions constitute the model we have chosen:

(1) F atoms are produced by

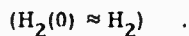
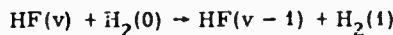
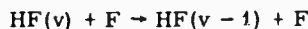


(2) vibrationally excited HF is produced by



(3) Only HF levels with v < 3 are produced and relaxation processes involving v > 3 are negligible.

(4) The dominant relaxation processes are:



(5) Rotational relaxation is sufficiently fast so that the rotational energy distribution is thermal with the rotational temperature equal to the translational temperature.

Under these assumptions, the controlling differential equations are:

$$(1) \frac{dF}{dt} = \frac{\sigma}{e} J(t) (SF_6) - k_t H_2 F$$

$$(2) \frac{d(SF_6)}{dt} = - \frac{\sigma}{e} J(t) (SF_6)$$

$$(3) \frac{dH_2}{dt} = -k_t H_2 F$$

$$(4) \frac{dn_3}{dt} = k_3 H_2 F - \lambda_3 n_3 n - \gamma_3 n_3 F + k_{f2} n_2^2 - k_{b2} n_3 n_1 + k_{f12} n_1 n_2 \\ - k_{b12} n_0 n_3 - k_{H_{23}} n_3 H_2 - S_{32}$$

$$(5) \frac{dn_2}{dt} = k_2 H_2 F + \lambda_3 n_3 n - \lambda_2 n_2 n + \gamma_3 n_3 F - \gamma_2 n_2 F + k_{f1} n_1^2 - 2k_{f2} n_2^2 \\ + 2k_{b2} n_3 n_1 - k_{b1} n_2 n_0 - k_{f12} n_1 n_2 + k_{b12} n_0 n_3 + k_{H_{23}} n_3 H_2 \\ - k_{H_{22}} n_2 H_2 + S_{32} - S_{21}$$

$$(6) \frac{dn_1}{dt} = k_1 H_2 F + \lambda_2 n_2 n - \lambda_1 n_1 n + \gamma_2 n_2 F - \gamma_1 n_1 F + k_{f2} n_2^2 - 2k_{f1} n_1^2 \\ + 2k_{b1} n_0 n_2 - k_{b2} n_1 n_3 - k_{f12} n_1 n_2 + k_{b12} n_0 n_3 + k_{H_{22}} n_2 H_2 \\ - k_{H_{21}} n_1 H_2 + S_{21} - S_{10}$$

$$(7) \frac{dn_0}{dt} = k_0 H_2 F + \lambda_1 n_1 n + \gamma_1 n_1 F + k_{f1} n_1^2 - k_{b1} n_0 n_2 + k_{f12} n_1 n_2 \\ - k_{b12} n_0 n_3 + k_{H_{21}} n_1 H_2 + S_{10}$$

where

$$n = n_0 + n_1 + n_2 + n_3$$

$$k_t = k_1 + k_2 + k_3 + k_4$$

and

$$S_{v,v-1} = \frac{\lambda_{v,v-1}^2 \Phi_{v,v-1} B(2J_v + 1)}{4\pi^2 kT E_{v,v-1} \Delta\nu_{v,v-1} \tau_{v,v-1}} \left\{ n_v \exp\left(\frac{-BJ_v(J_v - 1)}{kT}\right) - n_{v-1} \exp\left(\frac{-BJ_{v-1}(J_{v-1} + 1)}{kT}\right) \right\}$$

where  $J_{v-1} + J_v + 1$  for  $v = 1, 2$ , and 3 are,

$$(8), (9), (10) \quad \frac{d\Phi_{v,v-1}}{dt} = e\Phi_{v,v-1} \left[ \frac{t\lambda_{v,v-1}^2 B(2J_v + 1)}{d4\pi^2 \Delta\nu_{v,v-1} \tau_{v,v-1} kT} \right. \\ \cdot \left\{ n_v \exp\left(\frac{-BJ_v(J_v + 1)}{kT}\right) - n_{v-1} \exp\left(\frac{-BJ_{v-1}(J_{v-1} + 1)}{kT}\right) \right\} \\ + \frac{1}{2d} \ln(1 - K) \left] + fI \frac{dn_v}{dt} - \frac{E_{v,v-1}}{\tau_{v,v-1}} \frac{B}{kT} (2J_v + 1) \exp\left(\frac{-BJ_v(J_v + 1)}{kT}\right) \right]$$

Also,

$$\Phi = \Phi_{32} + \Phi_{21} + \Phi_{10}$$

$$\Phi_{out} = \frac{K}{2-K} \Phi$$

Definitions:

$t$	time
$F$	fluorine atom concentration
$\sigma$	cross section for dissociation of F from $SF_6$ by an electron
$J(t)$	electron current density
$e$	electron charge
$k_t$	total rate constant for $F + H_2 \rightarrow HF + H$
$H_2$	$H_2$ concentration
$SF_6$	$SF_6$ concentration
$n_v$	concentration of HF with vibrational quantum number $v$
$k_v$	rate constant for $F + H_2 \rightarrow HF(v) + H$
$n$	total HF concentration
$\lambda_v$	rate constant for $HF(v) + HF \rightarrow HF(v-1) + HF$
$\gamma_v$	rate constant for $HF(v) + F \rightarrow HF(v-1) + F$
$\gamma_{fv}$	forward rate constant for $2 HF(v) \rightleftharpoons HF(v-1) + HF(v+1)$

$k_{bv}$	backward rate constant for $2 \text{ HF}(v) \rightleftharpoons \text{HF}(v-1) + \text{HF}(v+1)$
$k_{H_2v}$	rate constant for $\text{H}_2(0) + \text{HF}(v) \rightarrow \text{H}_2(1) + \text{HF}(v-1)$
$k_{f12}$	forward rate constant for $\text{HF}(1) + \text{HF}(2) \rightarrow \text{HF}(0) + \text{HF}(3)$
$k_{b12}$	backward rate constant for above
$\lambda_{v,v-1}$	wavelength of $v \rightarrow v-1$ transition
$\Phi_{v,v-1}$	laser intensity inside cavity in $v \rightarrow v-1$ transition; $\Phi$ = total intensity in cavity; $\Phi_{out}$ = output intensity.
B	rotational energy constant
$J_v$	rotational quantum number of upper state of $v \rightarrow v-1$ transition
k	Boltzmann constant
T	translational temperature
$E_{v,v-1}$	energy of $v \rightarrow v-1$ transition
$\Delta\nu_{v,v-1}$	Lorentz width of $v \rightarrow v-1$ transition
$\tau_{v,v-1}$	spontaneous emission time constant for $v \rightarrow v-1$ transition
c	speed of light
$l$	length of gain medium
d	cavity length
K	output coupling fraction
$\omega_e$	vibration energy constant for HF
$\omega_e^x$	anharmonic correction to HF vibrational energy
f	fraction of spontaneous emission in solid angle contributing to oscillation buildup

A program is presently being written to solve this set of first-order, second-degree differential equations. The Runge-Kutta integration method is being used.

S. Marcus  
D. L. Mooney

#### f. CO<sub>2</sub> Isotope Laser Measurements

We have previously reported a brief summary of our experiments on <sup>12</sup>C<sup>18</sup>O<sub>2</sub>, <sup>13</sup>C<sup>16</sup>O<sub>2</sub>, and <sup>13</sup>C<sup>18</sup>O<sub>2</sub> isotope laser. Detailed description of these experiments and the results will be published in the February 1974 issue of the Journal of Molecular Spectroscopy.

We have obtained laser action in <sup>12</sup>C<sup>16</sup>O<sup>18</sup>O and <sup>13</sup>C<sup>16</sup>O<sup>18</sup>O isotopes and obtained some preliminary data. Because of the vast number of lines obtainable in the mixed isotopes, identification is a more tedious process. To alleviate this problem and to obtain more accurate

measurements, the final results will be obtained with the lasers locked to the standing-wave saturation resonances observed in low-pressure CO<sub>2</sub> absorption cells, utilizing the upper to ground state spontaneous emission band at 4.3 μm. Appropriate external cell stabilization set-ups have been designed and built.

The design of the grating-controlled lasers has been improved. The previously troublesome output mode distortions have been eliminated, and also a large number of additional lasing transitions were observed.

C. Freed

#### REFERENCES

1. P. Kafalas and J. Herrmann, Optics Research Report, Lincoln Laboratory, M.I.T. (1971:2), pp. 21-23, DDC AD-901213-L.
2. C. E. Junge, Air Chemistry and Radioactivity (Academic Press, New York, 1963).
3. Optics Research Report, Lincoln Laboratory, M.I.T. (1973:1), pp. 15-19.
4. L. C. Bradley and J. Herrmann, private communication.
5. K. A. Brueckner and S. Jorna, Phys. Rev. Lett. 17, 78 (1966); Phys. Rev. 164, 182 (1967).
6. N. M. Kroll and P. T. Helley, Phys. Rev. (A) 4, 763 (1971).
7. S. S. Rangnekar, Can. J. Phys. 49, 1994 (1971).
8. D. Deirmendjian, "Scattering and Polarization Properties of Water Clouds and Hazes in the Visible and Infrared," Appl. Opt. 3 (February 1964).
9. F. S. Harris and F. L. Morse, Simultaneous Multichannel Sizing, Counting, and Recording of Aerosol Size Distributions," presented at the Atmospheric Optics Technical Group of the Optical Society of America, Pittsburg, Pennsylvania (October 1968); see also Technical Report 2476-3, Electro-Science Laboratory, Ohio State University (2 April 1969).
10. L. C. Bradley and J. Herrmann, LTP-10, Lincoln Laboratory, M.I.T. (12 July 1971), DDC AD-902041-L.
11. Van de Hulst, Light Scattering by Small Particles / in Wiley & Sons, New York, 1964).
12. A. C. Selden, Brit. J. Appl. Phys. 18, 743 (1967).
13. R. W. O'Neil, H. Kleiman and J. E. Lowder, Appl. Phys. Lett. (to be published).
14. A. F. Haught, R. G. Meyerand and D. C. Smith, in Physics of Quantum Electronics, edited by P. L. Kelley, B. Lox and P. E. Tannenwald (McGraw-Hill, New York, 1966).
15. R. G. Tomlinson, E. K. Damon and H. T. Buscher in Ref. 14.
16. S. A. Akhmanov, A. I. Kourigin, M. M. Strukov and R. V. Kokhlov, JETP Letters, Vol. 1, 25 (1965).
17. D. E. Lencioni, Appl. Phys. Lett. 23, 12 (1973).
18. N. Kroll and K. M. Watson, Phys. Rev. (A) 5, 1883 (1972).
19. H. T. Buscher, R. G. Tomlinson and E. K. Damon, Phys. Rev. Letters 15, 847 (1965).
20. R. J. Hull, D. E. Lencioni and L. C. Marquet in Laser Interaction and Related Plasma Phenomena, Vol. II, edited by H. J. Schwartz and H. Hora (Plenum, New York, 1972).

21. D. E. Lencioni, L. C. Pettingill, 26th Gaseous Electronics Conference, Madison, Wisconsin, 16-19 October 1973.
22. S. Marcus, H. Kleiman, R. W. O'Neil and L. C. Pettingill, J. Appl. Phys. 44 (1973).
23. Y. P. Raizer, Sov. Phys. JETP 21, 1009 (1965).
24. S. Marcus, Appl. Phys. Lett. 21, 18 (1972).
25. R. W. O'Neil, H. Kleiman, L. C. Marquet, C. W. Kiteline, D. Northram, Appl. Opt. (to be published).
26. J. E. Lowder, D. E. Lencioni, T. W. Hilton and R. J. Hull, J. Appl. Phys. 44, 2759 (1973).
27. A. N. Pirri, Physics of Fluids 16, 1435 (1973).
28. P. E. Nielsen, "Momentum Transfer to Solid Targets in the Presence of Laser-Supported Detonation Waves," presented at the DoD Laser Effects Hardening Conference, Monterey, California (October 1973).
29. Darii Yakovlevich Svet, Thermal Radiation, translated from the Russian (Consultants Bureau, New York, 1965).
30. R. B. Hall, W. E. Maher and D. J. Nelson, "Laser-Supported Detonation Waves," presented at the DoD Laser Effects/Hardening Conference, Monterey, California (October 1973).
31. R. T. Brown and D. C. Smith, Appl. Phys. Lett. 22, 245 (1973).
32. P. Kafalas and A. P. Ferdinand, Jr., Appl. Opt. 12, 29-33 (January 1973).
33. P. Kafalas and J. Herrmann, Appl. Opt. 12 (April 1973).
34. R. M. Osgood and D. L. Mooney, "Study of H<sub>2</sub>-HF Laser," Lincoln Laboratory Internal Memorandum, 1973. This was presented in part at the 26th Annual Gaseous Electronics Conference, Madison, Wisconsin (October 1973).
35. D. R. Bates, ed., Atomic and Molecular Processes (Academic Press, New York, 1968), p. 208.
36. L. S. Frost and A. V. Phelps, Phys. Rev. 127, 1521 (1962).
37. W. Nighan, Phys. Rev. (A) 2, 1989 (1970).
38. G. I. Schultz, Phys. Rev. 135, A988 (1964).
39. C. P. Robinson, R. J. Jensen and A. Kolb, IEEE J. Quantum Electron. QE-9, 963 (1973).
40. E. L. Patterson, R. A. Geroer, Sandia Laboratories Internal Report SLA-73-0861 (May 1973).

## II. OPTICAL MEASUREMENTS AND INSTRUMENTATION

### A. TRIANGULAR SCANNING MTF INTERFEROMETER

#### 1. MTF Interferometric Measurements

Two engineered models of the triangular scanning MTF interferometer<sup>1</sup> have now been built to our design by Infrared Industries for M.I.T. Lincoln Laboratory. It is suitable for field use, with provision for simple visual alignment by means of a reticle in an eyepiece. A camera can be attached to photograph interferograms. A dove prism to rotate the wavefront has been fitted in front of the entrance aperture. A flip mirror switches from visual examination to photoelectric detection. The shear plate in normal operation is continuously rotated at 3600 rpm by a motor, but can also be manually turned or locked in position at any particular shear value (motor switched off). An optical encoder keeps track of the angular position of the shear plate, providing indexing pulses once per revolution, together with a continuous 200-kHz digital output. These two encoder data allow indexing of the zero shear position in the MTF data as well as very accurate shear (spatial frequency) axis calibration.

The MTF signal data and the two encoder data outputs are recorded on magnetic tape (having a high-frequency bandwidth), and the tapes subsequently digitized and fed to a computer for data reduction and statistical analysis of the data. The instrument measures and records 14,400 MTF curves each minute, and a complete MTF curve is made in 1.3 msec. A micrometer adjustment allows accurate rotation of the optical part of the triangular interferometer as a unit such that the carrier signal can be easily adjusted while operating the interferometer (from zero to about 100 kHz). The instrument has initially been designed for use with a HeNe CW laser source (632.8 nm). However, within certain spectral and spatial coherence limitations, it has been successfully tested with a small white incoherent source, using suitable bandwidth filters. We therefore expect to be able to look at star sources and measure the MTF at various slant paths through the whole of the atmosphere. The instrument can be converted to infrared wavelengths, and this is being done for a 10-micron version.

A photograph of the instrument is shown in Fig. II-1. Modular amplifiers and filters are used to provide simple electronic processing (mainly noise reduction and gain control) of the data signals for recording on tape. The interferometer accepts up to a 10-mm-diameter collimated light

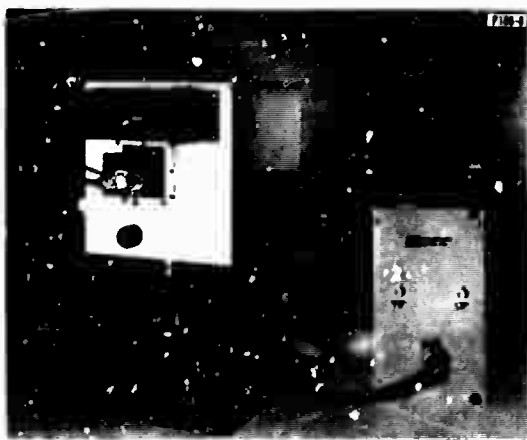


Fig. II-1. Fast-scanning MTF interferometer.

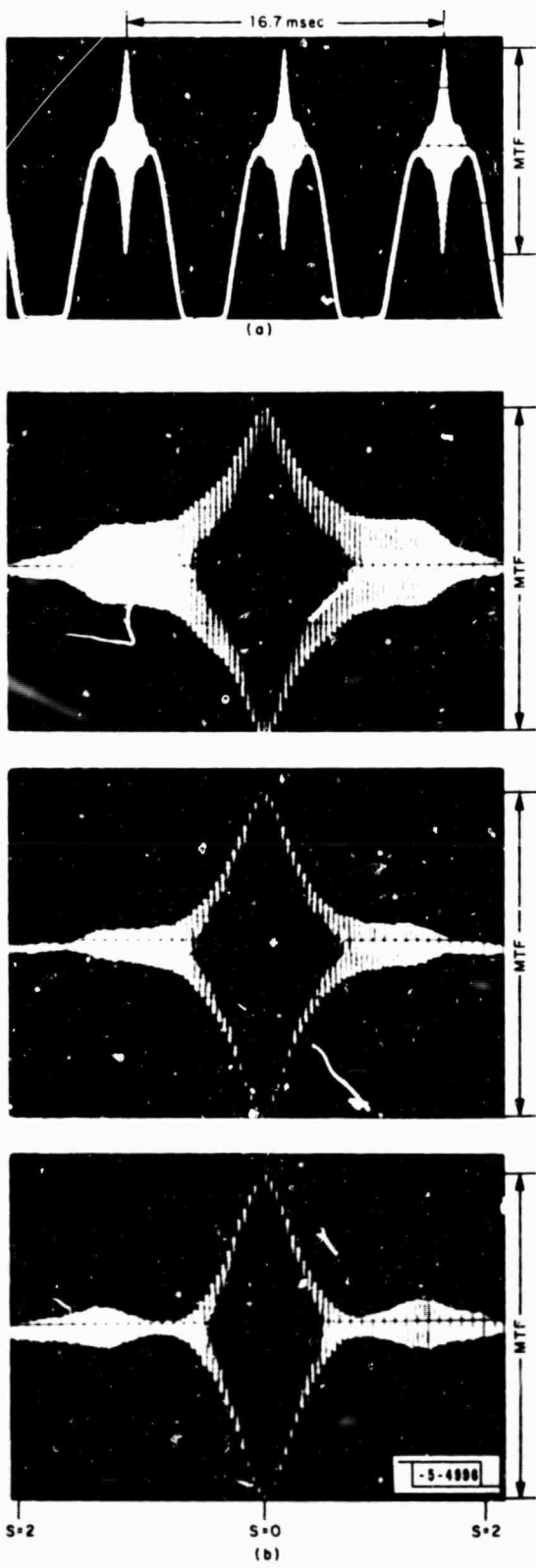


Fig. II-2. (a) Interferometer output (6 curves), (b) MTF in laboratory: Typical variations for 14-meter path (6 curves) (the limiting resolution at  $s = 2$  corresponds here to about 110 cycles/mm).

beam. As an illustration of the MTF output from the interferometer, an 89-mm-diameter Questar telescope was used as a receiver, and a laser beam propagated over a 14-meter path in the air-conditioned laboratory. Figure II-2(a) shows the type of output obtained recorded on tape (6 MTF curves are shown), and for detailed examination, can be expanded as shown by the series in Fig. II-2(b). Typically, fluctuations in the temperature in the laboratory air produce the variations shown between the curves (these three pairs of curves in Fig. II-2(b) were selected at about one-minute intervals). The curves change slowly under these conditions. If now laboratory air is blown across in front of the aperture of the telescope, the MTF curve does not significantly change its characteristics, as shown in Fig. II-3(a). However, if temperature fluctuations are now introduced into this layer of air blown in front of the telescope (by including a heated coil in the blower), the MTF curve collapses, as shown in the three pairs of curves of Fig. II-3(b). The three pairs of curves were selected at about one-minute intervals.

In summary, large masses of slow-moving air from the air conditioner and people moving about the laboratory are causing slow variations, but not drastic collapse, of the MTF curve in Fig. II-2(b). A fast flow of ambient air (from a hair dryer located three feet away), about two feet in front of the telescope, produces no change in the nature or level of the MTF curve unless the heat is turned on to introduce large rapid temperature fluctuations, as shown in Fig. II-3(b). In this latter case, the MTF collapses and fluctuates (at high shear) rapidly. The two main examples illustrated are intended to demonstrate the type of effect on the MTF produced by long-path propagation through the atmosphere and propagation through a flight boundary layer, respectively.<sup>2</sup> Clearly, a more detailed simulation and analysis is called for in order to obtain realistic and accurate results. We are using statistical methods of analysis applied to the large number of MTF curves that can be measured in this way, to evaluate "mean," "peak," "minimum" MTF curves, and variance of the MTF amplitude at each shear value in order to characterize both the boundary layer in the flight tests and the long-path propagation problem.

## 2. Angle-of-Arrival and Nonimaging Tracker Application of the Interferometer

Optical trackers are usually based upon controlling and measuring the position of an image on a suitable sensor by some optical means (such as mosaic detector arrays or rotating reticles). However, an alternative interferometric nonimaging technique can be used and will be outlined here. The angle of arrival of an optical wave can be measured or tracked by means of the differential path change in a two-beam shearing interferometer. (For example, see Baker<sup>3</sup> and Dyson<sup>4</sup>)

In practice, the corner cube<sup>5</sup> and the triangular<sup>6</sup> shearing interferometers can be used for angle-of-arrival measurements and for tracking objects. The pointing sensitivity of the corner-cube interferometer has been analyzed by the writer<sup>5</sup> and particular application of this technique to tracking is discussed in the AFWL semiannual report.<sup>6</sup>

A different and very simple technique is possible using the triangular interferometer, and will be described here. The relationship between the differential path change for the two beams traversing the opposite paths in the triangular interferometer and the angle between the two beams  $\delta\theta$  is given by<sup>1</sup>

$$\Delta = \frac{(\mu - 1)t}{2\mu} (\theta_1 + \theta_2) \delta\theta . \quad (II-1)$$

The angle  $\delta\theta$  is, in practice, equal to the pointing angle. (This is the direction the incoming beam to the interferometer makes with the beam that would traverse the interferometer exactly

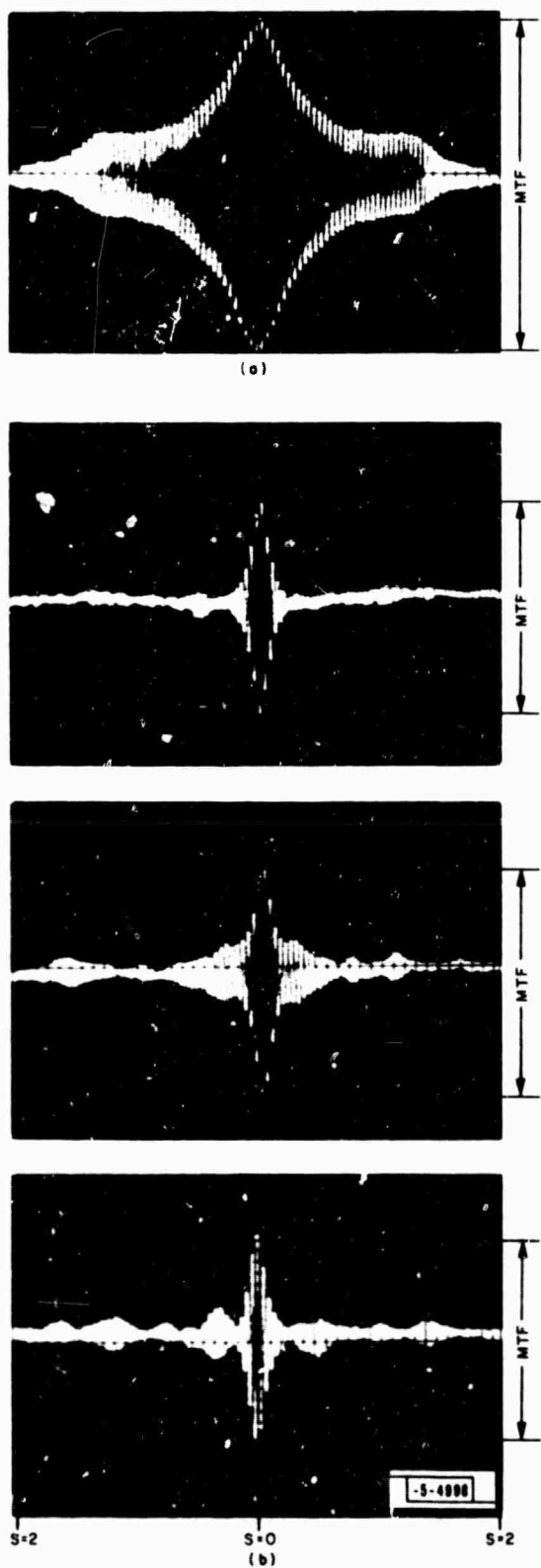


Fig. II-3. Laboratory boundary layer simulation: (a) ambient air temperature wind (2 curves), (b) hot air temperature wind (6 curves).

symmetrically.) In operation, the shear plate is continuously rotated at a fixed speed, and the carrier signal frequency produced is given by  $f = \partial\Delta/\partial t$  or, from the above expression,

$$f = \frac{(\mu - 1)t}{2\mu} \frac{\partial\theta}{\partial t} + \delta\theta . \quad (\text{II-2})$$

Therefore, keeping  $\partial\theta/\partial t$  constant, depending on the motor speed, the carrier signal frequency is proportional to the pointing angle  $\delta\theta$ . If the interferometer is therefore rigidly fixed in a mount, the angle of arrival of a wavefront can be monitored simply by measuring the frequency modulation of the carrier signal. In this respect, one very important advantage of this technique is that the signal amplitude fluctuations due to both scintillation and to phase degradation through the atmospheric path do not influence the measurement and do not change the carrier frequency.

To make use of this method for application to an optical tracker, the interferometer pointing direction can be controlled by a servomechanism to reduce the carrier signal  $f$  to zero and keep it there so that the pointing angle  $\delta\theta$  will be zero. The magnitude of the minimum angle of arrival (or tracking error) that can be anticipated by this technique can be estimated by using Eq. (II-1). The minimum angle-of-arrival sensitivity will be given by

$$\delta\theta_{\min} = \frac{2\mu}{(\mu - 1)t} \times \frac{\Delta_{\min}}{(\theta_1 + \theta_2)} .$$

where  $\Delta_{\min}$  can, for example, be taken as one-tenth wave,  $\mu = 1.5$ ,  $t = 2.5$  cm, and  $\theta_1 \approx \theta_2 = 40^\circ$ , and  $\lambda = 632.8$  nm. The angular sensitivity is thus

$$\delta\theta_{\min} \approx 10^{-5} \quad \text{or} \quad 2 \text{ sec of arc} .$$

This tolerance is calculated for the case where the interferometer is used without any pre-optics (an 8-mm input beam). Using the 89-mm-diameter Questar telescope produces an equivalent ten times magnification in the angular sensitivity, which will be roughly two-tenths second of arc overall sensitivity. Longer focal-length optics will allow correspondingly larger magnifications. It is clear that with this sensitivity to pointing, rigid mounting of this equipment is mandatory.

A demonstration of this technique was performed in the laboratory with the 89-mm-diameter Questar telescope and the triangular interferometer. The laser source (with a diverging lens) was located about 14 meters from the telescope. A small 0.95-cm-thick optical plate was placed close to and in front of the source on a rotatable table. One-degree rotation of the table produces a small lateral shift of the source, so that the laser beam direction as seen from the telescope changes by one second of arc. This was a very sensitive way of changing the angular direction of the laser beam into the Questar telescope and interferometer systems. A series of interferometer outputs was obtained, shown in Fig. II-4, as the angular direction changed through the exact "on axis" position and beyond, up to about 28 seconds of arc off the axis. The carrier frequency decreases linearly with this angle. The signal frequency modulation is zero at the on-axis position. The width of each picture (each double curve) in Fig. II-4 is about 3 msec. Hence, fast response in an FM tracking mode is quite feasible. There is some dead time between curves with this technique, but three stacked channels in one interferometer could be used to overcome this. While this provides tracking along one axis, a similar interferometer stack can be used to provide tracking in a mutually orthogonal direction. The system has been provisionally tested in the laboratory with an incoherent light source (and suitable bandwidth filters) and performs satisfactorily in this mode, but with less sensitivity. At a later date, an infrared system will be tested.

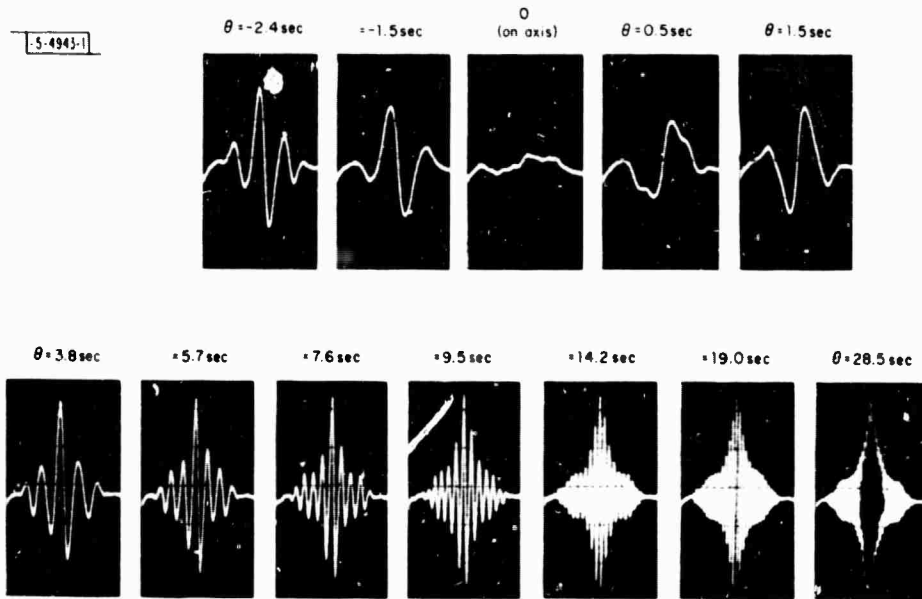


Fig. II-4. Interferometer output for different angle-of-arrivals ( $\theta$ ) (using 89-mm Questar telescope).

#### REFERENCES

1. D. Kelsall, *Appl. Opt.* **12**, 1398 (1973).
2. Optics Research Report, Lincoln Laboratory, M.I.T. (1972-1), p. 62, DDC AD-754939.
3. L. R. Baker, *Proc. Phys. Soc.* **68B**, 871 (1955).
4. J. Dyson, *Optica Acta* **10**, 171 (1963).
5. D. Kelsall, *J. Opt. Soc. Am.* **63**, 1472 (1973).
6. Semiannual Report, AFWL (March 1973), p. 9.